The Astrophysical Journal, 855:140 (21pp), 2018 March 10 https://doi.org/10.3847/1538-4357/aaac7e

MMT Spectroscopy of Supernova Remnant Candidates in M33

Knox S. Long[1,2], William P. Blair[3], Dan Milisavljevic[4,5], John C. Raymond[5], and P. Frank Winkler[6]
[1] Space Telescope Science Institute, 3700 San Martin Drive, Baltimore MD 21218, USA; long@stsci.edu
[2] Eureka Scientific, Inc. 2452 Delmer Street, Suite 100, Oakland, CA 94602-3017, USA
[3] The Henry A. Rowland Department of Physics and Astronomy, Johns Hopkins University, 3400 N. Charles Street, Baltimore, MD 21218, USA; wpb@pha.jhu.edu
[4] Department of Physics and Astronomy, Purdue University, 525 Northwestern Avenue, West Lafayette, IN 47907, USA; dmilisav@purdue.edu
[5] Harvard-Smithsonian Center for Astrophysics, 60 Garden Street, Cambridge, MA 02138, USA; jraymond@cfa.harvard.edu
[6] Department of Physics, Middlebury College, Middlebury, VT 05753, USA; winkler@middlebury.edu
Received 2017 December 18; revised 2018 January 26; accepted 2018 January 28; published 2018 March 16

Abstract

To date, over 220 emission nebulae in M33 have been identified as supernova remnants (SNRs) or SNR candidates, principally through [S II]:Hα line ratios that are elevated compared to those in H II regions. In many cases, the determination of a high [S II]:Hα line ratio was made using narrow-band interference filter images and has not been confirmed spectroscopically. Here, we present MMT 6.5 m optical spectra that we use to measure [S II]:Hα and other line ratios in an attempt to determine the nature of these suggested candidates. Of the 197 objects in our sample, 120 have no previously published spectroscopic observations. We confirm that the majority of candidate SNRs have emission line ratios characteristic of SNRs. While no candidates show Doppler-broadened lines expected from young, ejecta-dominated SNRs ($\gtrsim$1000 km s^{-1}), a substantial number do exhibit lines that are broader than H II regions. We argue that the majority of the objects with high [S II]:Hα line ratios (>0.4) are indeed SNRs, but the distinction between H II regions and SNRs becomes less obvious at low surface brightness, and additional criteria, such as X-ray detection, are needed. We discuss the properties of the sample as a whole and compare it with similar samples in other nearby galaxies.

Key words: galaxies: individual (M33) – ISM: supernova remnants

Supporting material: machine-readable tables

1. Introduction

Although most Galactic supernova remnants (SNRs) were first identified as extended sources of non-thermal radio emission, most extragalactic SNRs have been identified through interference filter imaging as emission nebulae with [S II] $\lambda\lambda$6717, 6731:Hα line ratios that are elevated compared to those in H II regions (see, e.g., Long 2017, and references therein). In H II regions, particularly those of high surface brightness, the observed [S II]:Hα ratios are typically of order 0.1 because most sulfur is photoionized to S^{++}. In contrast, most SNRs are observed to have [S II]:Hα ratios of at least 0.4 because sulfur is found in a wide variety of ionization states in the extended recombination zone behind radiative shocks. This expectation has support from a long series of radiative shock model calculations that generally confirm this expectation (e.g., Raymond 1979; Hartigan et al. 1987; Dopita & Sutherland 1995; Allen et al. 2008).

The reason that most extragalactic SNRs have been identified optically reflects the history of relative sensitivity of optical, radio, and X-ray searches for SNRs in external galaxies. M33, at a distance of 817 $\pm$ 58 kpc (Freedman et al. 2001), was one of the first galaxies where a search for SNRs was carried out. The first three SNRs there were identified by D'Odorico et al. (1978) and then confirmed spectroscopically by Dopita et al. (1980). Additional searches followed as instrumentation improved, in particular with the advent of CCDs (Long et al. 1990; Gordon et al. 1998), such that there were approximately 100 SNR candidates known in M33 by the turn of the century. Most recently Long et al. (2010; hereafter Long10) and Lee & Lee (2014b; hereafter LL14) identified 137 and 199 partially overlapping sets of SNRs in M33, respectively, both from an examination of interference filter images obtained by Massey et al. (2006, 2007) as part a ground-based survey of Local Group galaxies.[7] It is not surprising that these two sets of candidates are not identical. Although both studies found the same *bright* SNR candidates, the criteria used to identify candidate SNRs become more subjective and confused at the faint end of the distribution. LL14 also surveyed extended regions in the northern and southern extremes of M33, beyond the region searched by Long10.

The brightest SNRs are apparent in [S II] and Hα images, but continuum images must be subtracted from the emission-line images in order to search effectively for fainter remnants. The subtraction is never perfect, due to changing seeing conditions and color terms associated with different stars. The initial selection of candidates is made by visual inspection, and extracting line ratios from the subtracted emission-line images is by no means straightforward. Additionally, different investigators adopt different criteria for determining what is a *bona fide* candidate, such as whether or not to require a certain morphology, exclude nebulae with interior blue stars, etc. Furthermore, the pass bands for the Hα interference filters used by different observers is important because virtually all such filters pass at least some of the [N II] $\lambda\lambda$6548, 6583 lines adjacent to Hα, "contaminating" the Hα images by varying amounts and thus lowering the apparent [S II]:Hα ratio. For all of these reasons and more, it is important to obtain spectra of as many of the SNR candidates as possible to clarify their status. As summarized by Long10, spectra of 85 of the 137 then-known SNRs or candidates had been obtained, with a variety of instrumentation.

[7] Long10 also used a set of somewhat deeper but lower-resolution images from the 0.6 m Burrell Schmidt telescope, in addition to the LGGS.

In this paper, we describe a new spectroscopic study of the SNR candidates in M33. Our goals were: to obtain spectra of as many of the SNRs as possible with the same instrumental setup; to include as many as possible of the fainter SNR candidates, particularly those not observed previously, in order to obtain accurate [S II]:Hα ratios; and, inasmuch as possible, determine the status of the SNR candidates.

2. Observations and Data Reduction

In order to define our observing program, we first created a combined set of targets from the list of objects contained in Long10 and LL14. This was necessary because the LL14 list is not a simple superset of the list of Long10. LL14 eliminated a number of sources from their consideration because they argued the sources were too large or not "SNR-like" enough in morphology to be considered SNRs. They also remeasured source positions and concluded that some candidates were associated with a somewhat different set of filaments than Long10 had identified. In identifying SNR positions, we adopted the following (somewhat parochial) strategy of favoring positions from Long10. We assumed that an SNR identified by LL14 was the same SNR as identified by Long10, if the position was within 3″ of a Long10 SNR. By this criterion, 119 of the 199 LL14 SNRs correspond to Long10 SNRs, and thus there are 80 LL14 SNRs that are not in the Long10 list. There are also 18 Long10 SNRs not in the LL14 list. Thus, our initial sample comprised 217 objects, whose positions are shown on an Hα image of the galaxy in Figure 1. Recently, Garofali et al. (2017) compiled their own list of SNRs from Long10 and LL14 and elsewhere. Their list has 218 objects, three of which—XMM-081, XMM-089, and XMM-095—were not identified either by Long10 or LL14, and have no associated optical counterparts, based on our inspection of the LGGS images. Garofali et al. (2017) also do not include two objects which we have listed as separate objects here: LL14-096 and LL14-174.

Some basic supporting data about the 217 objects for the purpose of this discussion are presented in Table 1. This table contains: (1) the source name we use for the object in this paper, (2, 3) the position of the object, (4) the apparent size of the object in pc, (5) the galactocentric distance (GCD) of the object in kpc, (6) the name of the object in Long10, (7) the name of the object in LL14, (8) whether the object has been detected in X-rays, (9) the reference to previous spectra of the the object, (10) whether we acquired a new spectrum, and (11) whether or not the spectra indicate that [S II]:Hα ratio was greater than or equal to 0.4. In creating the table, we have taken names and data from Long10 if the object existed in Long10 and used data from LL14 for the remainder. We have not remeasured the apparent diameters of the objects. For the purpose of this discussion, we have listed an object as X-ray detected if the significance of the detection was 3σ with *Chandra* by Long10 or with *XMM-Newton* by Garofali et al. (2017). We record an object as [S II]:Hα confirmed if we find an [S II]:Hα ratio greater than or equal to 0.4, or if it was not observed by us but previous observers have reported a similarly high ratio. Objects with no entry in this column are objects without (to the best of our knowledge) any previous spectroscopic follow-up.

Our new spectroscopic observations were carried out with Hectospec (Fabricant et al. 2005), a moderate-resolution (~5 Å), multi-fiber spectrograph available on the 6.5 m MMT. We used the 270 lines mm^{-1} grating, which gives a total spectral coverage of 3600–9100 Å. Each fiber has a core diameter on the sky of 1.″5, spanning ≈6 pc at the 817 kpc distance of M33.

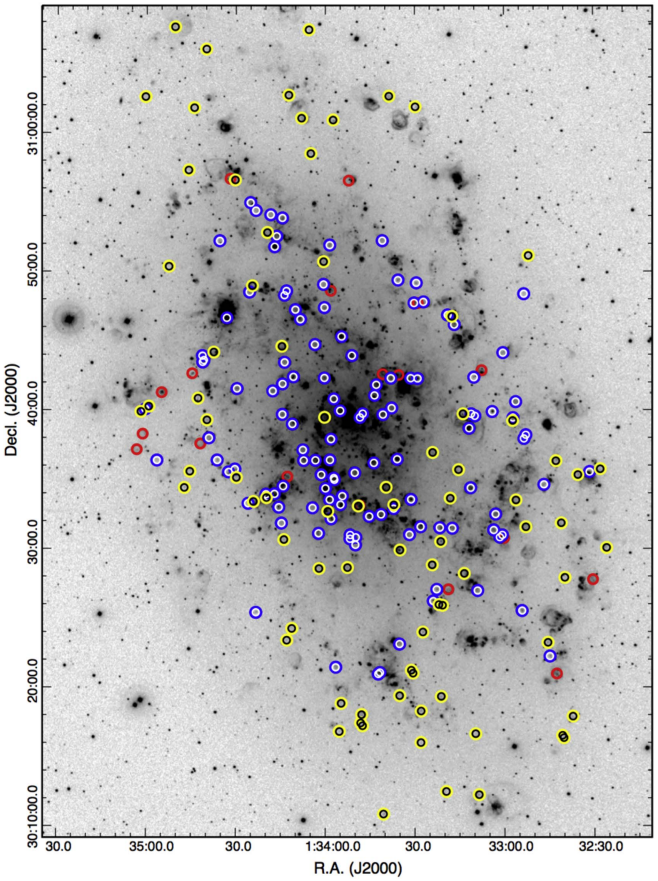

Figure 1. An image of M33 from the 0.6 m Burrell Schmidt telescope at KPNO, with the positions of the SNRs and SNR candidates indicated as follows: blue/white circles indicate objects that appear in both the L10 and LL14 catalogs; red circles are ones that appear only in L10; and yellow/black circles are ones that appear only in LL14. The field size is 44′ × 60′, oriented north up, east left.

The observations took place over eight nights in 2016 October and November, under good conditions. We obtained spectra of 197 out of the list of 217 objects: 110 objects in both lists, 18 objects in the Long10-only list, and 69 objects in the LL14-only list. For comparison purposes, we also obtained spectra of 23 bright H II regions, but because a far larger spectroscopic survey of H II regions in M33 has recently been reported by (Lin et al. 2017, hereafter Lin17), we have used our own H II region spectra only for estimating instrumental line widths. Individual exposures of 1800 s were obtained and combined to create total exposures that varied from ~2 to 10 hr per target.

All of the data were reduced using the standard Hectospec pipeline (HSRed Version 2.0),[8] which applied wavelength calibration, performed cosmic-ray rejection, subtracted sky emission using >20 sky fibers that were averaged and scaled in intensity, and corrected for telluric absorption features. For flux calibration, we used multiple observations of the spectrophotometric standard star BD+28-4211. Many of the objects were observed multiple times. Because the spectra of individual objects observed over multiple nights were similar, we

[8] https://www.mmto.org/node/536

Table 1
SNR Candidates in M33

Source	R.A. (2000)	Decl. (2000)	Diameter (pc)	ρ (kpc)	L10	LL14	XMM	X-Ray Detected	Previous Spectrum	New Spectrum	[S II]:Hα Confirmed
L10-001	01:32:30.37	30:27:46.9	126	6.5	L10-001	…	XMM-003	yes	G98	yes	yes
L10-002	01:32:31.41	30:35:32.9	33	6.5	L10-002	LL14-003	XMM-004	yes	G98	yes	yes
L10-003	01:32:42.54	30:20:58.9	104	6.1	L10-003	…	XMM-011	no	G98	yes	yes
L10-004	01:32:44.83	30:22:14.6	42	5.8	L10-004	LL14-011	XMM-013	no	…	yes	yes
L10-005	01:32:46.73	30:34:37.8	49	5.2	L10-005	LL14-013	XMM-015	yes	L10	yes	yes
L10-006	01:32:52.76	30:38:12.6	60	4.9	L10-006	LL14-015	XMM-017	yes	S93	yes	yes
L10-007	01:32:53.36	30:48:23.1	77	6.3	L10-007	LL14-018	XMM-019	yes	…	yes	yes
L10-008	01:32:53.40	30:37:56.9	55	4.8	L10-008	LL14-017	XMM-020	no	S93	yes	yes
L10-009	01:32:54.10	30:25:31.8	42	4.9	L10-009	LL14-019	XMM-021	no	…	yes	yes
L10-010	01:32:56.15	30:40:36.4	97	4.9	L10-010	LL14-021	XMM-022	yes	S93	yes	yes
L10-011	01:32:57.07	30:39:27.1	23	4.7	L10-011	LL14-022	XMM-024	yes	L10	yes	yes
L10-012	01:33:00.15	30:30:46.2	56	4.1	L10-012	…	XMM-026	yes	…	yes	yes
L10-013	01:33:00.42	30:44:08.1	37	5.0	L10-013	LL14-024	XMM-027	yes	G98	yes	yes
L10-014	01:33:00.67	30:30:59.3	49	4.1	L10-014	LL14-025	XMM-028	no	…	yes	yes
L10-015	01:33:01.51	30:30:49.6	32	4.0	L10-015	LL14-026	XMM-029	no	…	no	…
L10-016	01:33:02.93	30:32:29.6	55	3.9	L10-016	LL14-027	XMM-030	yes	L10	yes	yes
L10-017	01:33:03.57	30:31:20.9	36	3.8	L10-017	LL14-028	XMM-031	yes	G98	no	yes
L10-018	01:33:04.03	30:39:53.7	34	4.1	L10-018	LL14-029	XMM-032	yes	S93	yes	yes
L10-019	01:33:07.55	30:42:52.5	74	4.2	L10-019	…	XMM-033	yes	…	yes	yes
L10-020	01:33:08.98	30:26:58.9	55	3.9	L10-020	LL14-031	XMM-035	yes	…	yes	yes
L10-021	01:33:09.87	30:39:34.9	70	3.6	L10-021	LL14-033	XMM-037	no	S93	no	yes
L10-022	01:33:10.18	30:42:22.0	31	3.9	L10-022	LL14-034	XMM-038	yes	L10	yes	yes
L10-023	01:33:11.10	30:39:43.7	29	3.5	L10-023	LL14-035	XMM-039	yes	L10	yes	yes
L10-024	01:33:11.28	30:34:23.5	102	3.2	L10-024	LL14-036	XMM-040	no	S93	yes	yes
L10-025	01:33:11.76	30:38:41.5	28	3.3	L10-025	LL14-037	XMM-041	yes	L10	yes	yes
L10-026	01:33:16.73	30:46:10.3	77	4.0	L10-026	LL14-041	XMM-045	no	…	yes	yes
L10-027	01:33:17.44	30:31:28.5	48	2.9	L10-027	LL14-042	XMM-046	yes	G98	yes	yes
L10-028	01:33:18.80	30:27:04.4	183	3.5	L10-028	…	XMM-049	no	…	yes	yes
L10-029	01:33:18.94	30:46:51.9	69	4.0	L10-029	LL14-045	XMM-050	yes	…	yes	yes
L10-030	01:33:21.64	30:31:31.1	79	2.6	L10-030	LL14-050	XMM-055	no	…	yes	yes
L10-031	01:33:22.67	30:27:04.0	23	3.3	L10-031	LL14-052	XMM-057	yes	L10	yes	yes
L10-032	01:33:23.85	30:26:13.5	25	3.5	L10-032	LL14-053	XMM-058	yes	BK85	yes	yes
L10-033	01:33:27.07	30:47:48.6	70	3.6	L10-033	LL14-056	XMM-061	no	L10	yes	yes
L10-034	01:33:28.08	30:31:35.0	36	2.3	L10-034	LL14-060	XMM-065	yes	G98	yes	yes
L10-035	01:33:28.96	30:47:43.5	22	3.4	L10-035	…	XMM-066	yes	L10	yes	no
L10-036	01:33:29.05	30:42:17.0	22	2.3	L10-036	LL14-061	XMM-067	yes	S93	yes	yes
L10-037	01:33:29.45	30:49:10.8	35	3.8	L10-037	LL14-062	XMM-068	yes	G98	yes	yes
L10-038	01:33:30.21	30:47:43.8	55	3.4	L10-038	LL14-064	XMM-070	no	L10	yes	yes
L10-039	01:33:31.25	30:33:33.4	16	1.9	L10-039	LL14-067	XMM-073	yes	L10	yes	yes
L10-040	01:33:31.34	30:42:18.3	58	2.1	L10-040	LL14-068	XMM-074	yes	S93	yes	no
L10-041	01:33:31.80	30:31:01.1	100	2.3	L10-041	LL14-069	XMM-075	yes	…	yes	yes
L10-042	01:33:35.14	30:23:07.5	46	4.1	L10-042	LL14-071	XMM-078	yes	…	yes	yes
L10-043	01:33:35.39	30:42:32.1	88	1.8	L10-043	…	XMM-079	yes	…	yes	yes
L10-044	01:33:35.61	30:49:23.0	32	3.4	L10-044	LL14-073	XMM-080	yes	L10	yes	yes
L10-045	01:33:35.90	30:36:27.4	33	1.2	L10-045	LL14-074	XMM-082	yes	L10	yes	yes
L10-046	01:33:37.09	30:32:53.5	42	1.8	L10-046	LL14-076	XMM-083	yes	L10	yes	yes
L10-047	01:33:37.75	30:40:09.2	53	1.2	L10-047	LL14-077	XMM-085	yes	S93	no	yes
L10-048	01:33:38.01	30:42:18.2	25	1.6	L10-048	LL14-078	XMM-086	no	S93	yes	yes
L10-049	01:33:40.66	30:39:40.8	46	0.9	L10-049	LL14-082	XMM-091	yes	…	yes	yes
L10-050	01:33:40.73	30:42:35.7	75	1.4	L10-050	…	XMM-092	no	S93	yes	yes
L10-051	01:33:40.87	30:52:13.7	64	3.9	L10-051	LL14-083	XMM-093	no	G98	yes	yes
L10-052	01:33:41.30	30:32:28.4	37	1.8	L10-052	LL14-084	XMM-094	no	…	yes	yes
L10-053	01:33:41.71	30:21:04.1	38	4.8	L10-053	LL14-085	XMM-096	no	G98	yes	yes
L10-054	01:33:42.24	30:20:57.8	49	4.8	L10-054	LL14-086	XMM-097	no	…	yes	yes
L10-055	01:33:42.91	30:41:49.5	48	1.1	L10-055	LL14-087	XMM-098	yes	…	yes	yes
L10-056	01:33:43.49	30:41:03.8	27	0.9	L10-056	LL14-088	XMM-099	yes	G98	no	yes
L10-057	01:33:43.70	30:36:11.5	40	0.9	L10-057	LL14-089	XMM-100	yes	S93	yes	yes
L10-058	01:33:45.26	30:32:20.1	71	1.8	L10-058	LL14-090	XMM-101	no	…	yes	yes
L10-059	01:33:47.46	30:39:44.7	45	0.3	L10-059	LL14-091	XMM-102	yes	…	yes	yes
L10-060	01:33:48.35	30:39:28.4	17	0.2	L10-060	LL14-095	XMM-106	no	G98	yes	yes
L10-061	01:33:48.50	30:33:07.9	63	1.7	L10-061	…	XMM-107	yes	S93	yes	yes
L10-062	01:33:49.75	30:30:49.7	76	2.4	L10-062	LL14-097	XMM-108	no	…	yes	yes

Table 1
(Continued)

Source	R.A. (2000)	Decl. (2000)	Diameter (pc)	ρ (kpc)	L10	LL14	XMM	X-Ray Detected	Previous Spectrum	New Spectrum	[S II]:Hα Confirmed
L10-063	01:33:49.90	30:30:16.7	57	2.5	L10-063	LL14-098	XMM-109	no	…	yes	yes
L10-064	01:33:50.12	30:35:28.6	52	1.1	L10-064	LL14-099	XMM-110	yes	S93	yes	yes
L10-065	01:33:51.06	30:43:56.2	53	1.2	L10-065	LL14-100	XMM-111	yes	S93	yes	yes
L10-066	01:33:51.67	30:30:59.6	63	2.4	L10-066	LL14-101	XMM-112	yes	G98	yes	yes
L10-067	01:33:51.71	30:30:43.4	49	2.5	L10-067	LL14-102	XMM-113	no	…	yes	yes
L10-068	01:33:52.15	30:56:33.4	112	4.6	L10-068	…	XMM-114	yes	…	yes	yes
L10-069	01:33:54.28	30:33:47.9	51	1.7	L10-069	LL14-104	XMM-116	yes	S93	yes	yes
L10-070	01:33:54.51	30:45:18.7	24	1.4	L10-070	LL14-105	XMM-118	yes	G98	yes	yes
L10-071	01:33:54.91	30:33:11.0	24	1.9	L10-071	LL14-107	XMM-119	yes	S93	yes	yes
L10-072	01:33:55.01	30:39:57.3	36	0.3	L10-072	LL14-108	XMM-120	no	…	yes	yes
L10-073	01:33:56.49	30:21:27.0	61	5.2	L10-073	LL14-110	XMM-122	yes	…	yes	yes
L10-074	01:33:56.97	30:34:58.7	34	1.6	L10-074	LL14-111	XMM-123	yes	L10	yes	yes
L10-075	01:33:57.13	30:40:48.5	48	0.5	L10-075	LL14-112	XMM-124	no	G98	yes	yes
L10-076	01:33:57.13	30:35:06.1	24	1.5	L10-076	LL14-113	XMM-125	no	…	yes	yes
L10-077	01:33:58.06	30:32:09.6	27	2.3	L10-077	LL14-115	XMM-127	yes	S93	yes	yes
L10-078	01:33:58.07	30:37:54.6	20	0.9	L10-078	LL14-116	XMM-128	yes	L10	yes	yes
L10-079	01:33:58.15	30:48:36.4	62	2.3	L10-079	…	XMM-130	yes	…	yes	yes
L10-080	01:33:58.42	30:36:24.3	11	1.3	L10-080	LL14-117	XMM-129	yes	L10	yes	yes
L10-081	01:33:58.51	30:33:32.3	38	2.0	L10-081	LL14-119	XMM-132	yes	S93	yes	yes
L10-082	01:33:58.52	30:51:54.3	60	3.1	L10-082	LL14-118	XMM-131	yes	G98	yes	yes
L10-083	01:33:59.93	30:34:21.2	34	1.9	L10-083	LL14-121	XMM-134	no	G98	no	yes
L10-084	01:34:00.31	30:42:19.4	36	0.9	L10-084	LL14-123	XMM-136	yes	L10	yes	yes
L10-085	01:34:00.32	30:47:24.1	46	1.9	L10-085	LL14-124	XMM-135	yes	…	yes	yes
L10-086	01:34:00.60	30:49:04.2	17	2.4	L10-086	LL14-126	XMM-139	yes	L10	yes	yes
L10-087	01:34:01.34	30:35:20.2	51	1.7	L10-087	LL14-127	XMM-140	yes	L10	yes	yes
L10-088	01:34:02.24	30:31:06.8	64	2.9	L10-088	LL14-129	XMM-142	yes	S93	yes	yes
L10-089	01:34:03.31	30:36:22.9	96	1.6	L10-089	LL14-130	XMM-143	yes	…	yes	yes
L10-090	01:34:03.48	30:44:43.8	45	1.4	L10-090	LL14-131	XMM-144	yes	S93	yes	yes
L10-091	01:34:04.26	30:32:57.1	40	2.5	L10-091	LL14-132	XMM-145	yes	…	yes	yes
L10-092	01:34:07.23	30:36:22.0	105	1.9	L10-092	LL14-135	XMM-148	yes	S93	yes	yes
L10-093	01:34:07.50	30:37:08.0	23	1.8	L10-093	LL14-136	XMM-149	yes	L10	yes	yes
L10-094	01:34:08.37	30:46:33.2	23	1.9	L10-094	LL14-138	XMM-151	yes	L10	yes	yes
L10-095	01:34:10.02	30:47:14.9	26	2.1	L10-095	LL14-139	XMM-152	yes	L10	no	yes
L10-096	01:34:10.70	30:42:24.0	22	1.6	L10-096	LL14-140	XMM-153	yes	S93	yes	yes
L10-097	01:34:11.04	30:38:59.9	18	1.8	L10-097	LL14-141	XMM-154	yes	G98	yes	yes
L10-098	01:34:12.69	30:35:12.0	70	2.6	L10-098	…	XMM-157	no	S93	yes	yes
L10-099	01:34:13.02	30:48:36.1	55	2.4	L10-099	LL14-145	XMM-159	yes	…	yes	yes
L10-100	01:34:13.65	30:43:27.0	29	1.8	L10-100	LL14-146	XMM-160	yes	S93	yes	yes
L10-101	01:34:13.71	30:48:17.5	61	2.4	L10-101	LL14-147	XMM-161	yes	…	yes	yes
L10-102	01:34:14.10	30:34:30.9	42	2.9	L10-102	LL14-149	XMM-163	yes	S93	no	yes
L10-103	01:34:14.35	30:41:53.6	51	1.9	L10-103	LL14-150	XMM-164	no	S93	yes	yes
L10-104	01:34:14.38	30:39:41.6	42	2.0	L10-104	LL14-151	XMM-166	yes	S93	yes	yes
L10-105	01:34:14.41	30:53:51.9	53	3.6	L10-105	LL14-152	XMM-165	yes	G98	yes	yes
L10-106	01:34:14.67	30:31:50.9	70	3.5	L10-106	LL14-154	XMM-168	yes	…	yes	yes
L10-107	01:34:15.57	30:32:59.9	37	3.3	L10-107	LL14-155	XMM-169	yes	S93	yes	yes
L10-108	01:34:16.31	30:52:32.7	80	3.3	L10-108	LL14-156	XMM-170	yes	L10	yes	yes
L10-109	01:34:17.00	30:51:47.1	29	3.2	L10-109	LL14-157	XMM-172	no	L10	yes	no
L10-110	01:34:17.03	30:33:57.7	57	3.2	L10-110	LL14-158	XMM-171	yes	…	yes	yes
L10-111	01:34:17.61	30:41:23.3	55	2.2	L10-111	LL14-159	XMM-173	yes	S93	yes	yes
L10-112	01:34:18.32	30:54:05.8	87	3.7	L10-112	LL14-160	XMM-174	no	…	yes	yes
L10-113	01:34:19.28	30:33:45.9	42	3.4	L10-113	LL14-161	XMM-175	no	S93	yes	yes
L10-114	01:34:19.87	30:33:56.0	26	3.4	L10-114	LL14-164	XMM-178	yes	S93	yes	yes
L10-115	01:34:23.23	30:25:24.9	51	5.6	L10-115	LL14-165	XMM-180	yes	…	yes	yes
L10-116	01:34:23.27	30:54:23.9	46	3.9	L10-116	LL14-166	XMM-179	yes	L10	yes	yes
L10-117	01:34:25.09	30:54:58.1	70	4.1	L10-117	LL14-169	XMM-183	yes	L10	yes	yes
L10-118	01:34:25.41	30:48:30.9	56	3.0	L10-118	LL14-170	XMM-184	yes	G98	yes	yes
L10-119	01:34:25.87	30:33:16.8	37	4.0	L10-119	LL14-171	XMM-185	yes	…	yes	yes
L10-120	01:34:29.61	30:41:33.4	47	3.2	L10-120	LL14-172	XMM-186	no	G98	yes	yes
L10-121	01:34:30.29	30:35:44.8	57	4.0	L10-121	LL14-175	XMM-188	yes	G98	yes	yes
L10-122	01:34:31.85	30:56:41.5	115	4.6	L10-122	…	XMM-189	yes	…	yes	yes
L10-123	01:34:32.41	30:35:32.6	44	4.2	L10-123	LL14-176	XMM-190	yes	…	yes	yes
L10-124	01:34:33.02	30:46:39.2	14	3.4	L10-124	LL14-177	XMM-191	yes	BK85	yes	yes

Table 1
(Continued)

Source	R.A. (2000)	Decl. (2000)	Diameter (pc)	ρ (kpc)	L10	LL14	XMM	X-Ray Detected	Previous Spectrum	New Spectrum	[S II]:Hα Confirmed
L10-125	01:34:35.41	30:52:12.7	42	4.0	L10-125	LL14-178	XMM-192	yes	…	yes	yes
L10-126	01:34:36.22	30:36:23.6	50	4.4	L10-126	LL14-179	XMM-193	no	…	yes	yes
L10-127	01:34:39.00	30:37:59.8	89	4.4	L10-127	LL14-181	XMM-195	yes	…	yes	yes
L10-128	01:34:40.73	30:43:36.4	26	4.0	L10-128	LL14-184	XMM-198	yes	L10	yes	yes
L10-129	01:34:41.10	30:43:28.3	43	4.1	L10-129	LL14-185	XMM-199	yes	BK85	no	yes
L10-130	01:34:41.23	30:43:55.4	38	4.1	L10-130	LL14-186	XMM-200	no	…	yes	yes
L10-131	01:34:41.89	30:37:35.2	159	4.7	L10-131	…	XMM-201	no	…	yes	yes
L10-132	01:34:44.62	30:42:38.8	58	4.4	L10-132	…	XMM-204	no	…	yes	no
L10-133	01:34:54.88	30:41:17.0	79	5.4	L10-133	…	XMM-210	no	…	yes	yes
L10-134	01:34:56.44	30:36:23.2	62	6.1	L10-134	LL14-194	XMM-211	no	…	yes	yes
L10-135	01:35:00.36	30:40:05.0	69	6.0	L10-135	LL14-197	XMM-214	no	…	yes	yes
L10-136	01:35:01.22	30:38:17.1	132	6.3	L10-136	…	XMM-216	no	…	yes	no
L10-137	01:35:03.18	30:37:09.6	130	6.6	L10-137	…	XMM-218	no	…	yes	yes
LL14-001	01:32:25.78	30:30:04.0	82	6.8	…	LL14-001	XMM-001	no	…	yes	yes
LL14-002	01:32:27.85	30:35:44.6	73	6.9	…	LL14-002	XMM-002	no	…	yes	yes
LL14-004	01:32:35.36	30:35:19.8	86	6.2	…	LL14-004	XMM-005	no	…	yes	no
LL14-005	01:32:37.16	30:17:54.3	86	6.8	…	LL14-005	XMM-006	yes	…	yes	no
LL14-006	01:32:39.78	30:27:55.0	36	5.7	…	LL14-006	XMM-007	no	…	yes	yes
LL14-007	01:32:40.23	30:16:21.3	44	6.9	…	LL14-007	XMM-008	no	…	yes	no
LL14-008	01:32:40.68	30:16:31.5	42	6.8	…	LL14-008	XMM-009	yes	…	yes	no
LL14-009	01:32:40.94	30:31:51.1	87	5.6	…	LL14-009	XMM-010	no	…	yes	no
LL14-010	01:32:42.71	30:36:20.1	59	5.6	…	LL14-010	XMM-012	no	…	yes	yes
LL14-012	01:32:45.47	30:23:14.2	45	5.7	…	LL14-012	XMM-014	no	…	yes	no
LL14-014	01:32:51.84	30:51:09.0	40	7.0	…	LL14-014	XMM-016	no	…	yes	no
LL14-016	01:32:52.80	30:31:34.2	69	4.7	…	LL14-016	XMM-018	no	…	yes	yes
LL14-020	01:32:56.12	30:33:30.4	81	4.4	…	LL14-020	XMM-023	yes	…	yes	yes
LL14-023	01:32:57.18	30:39:14.7	37	4.6	…	LL14-023	XMM-025	no	…	yes	no
LL14-030	01:33:08.55	30:12:15.2	27	6.9	…	LL14-030	XMM-034	yes	…	yes	yes
LL14-032	01:33:09.69	30:16:39.0	86	5.8	…	LL14-032	XMM-036	no	…	yes	no
LL14-038	01:33:13.46	30:28:13.1	75	3.5	…	LL14-038	XMM-042	yes	…	yes	yes
LL14-039	01:33:13.81	30:39:44.0	66	3.2	…	LL14-039	XMM-043	no	…	no	…
LL14-040	01:33:15.35	30:35:41.9	76	2.8	…	LL14-040	XMM-044	no	…	yes	yes
LL14-043	01:33:17.55	30:46:45.6	69	4.1	…	LL14-043	XMM-047	no	…	yes	yes
LL14-044	01:33:18.13	30:33:38.6	30	2.7	…	LL14-044	XMM-048	no	…	yes	yes
LL14-046	01:33:19.52	30:12:29.3	70	6.8	…	LL14-046	XMM-051	no	…	yes	no
LL14-047	01:33:20.76	30:25:55.2	16	3.6	…	LL14-047	XMM-052	no	…	yes	yes
LL14-048	01:33:21.19	30:19:20.6	75	5.1	…	LL14-048	XMM-053	no	…	yes	no
LL14-049	01:33:21.33	30:30:31.6	56	2.8	…	LL14-049	XMM-054	yes	…	yes	yes
LL14-051	01:33:21.94	30:25:58.4	36	3.6	…	LL14-051	XMM-056	no	…	yes	yes
LL14-054	01:33:24.01	30:36:56.8	77	2.2	…	LL14-054	XMM-059	yes	…	yes	yes
LL14-055	01:33:24.18	30:28:50.2	51	2.9	…	LL14-055	XMM-060	no	…	yes	yes
LL14-057	01:33:27.32	30:23:59.3	34	3.9	…	LL14-057	XMM-062	no	…	yes	no
LL14-058	01:33:27.92	30:18:17.4	40	5.3	…	LL14-058	XMM-063	no	…	yes	yes
LL14-059	01:33:28.00	30:16:01.2	37	5.9	…	LL14-059	XMM-064	no	…	yes	no
LL14-063	01:33:29.79	31:01:53.0	48	7.0	…	LL14-063	XMM-069	yes	…	yes	yes
LL14-065	01:33:30.64	30:21:01.5	89	4.7	…	LL14-065	XMM-071	no	…	yes	yes
LL14-066	01:33:31.20	30:21:14.3	59	4.6	…	LL14-066	XMM-072	no	…	no	…
LL14-070	01:33:35.10	30:19:24.2	64	5.1	…	LL14-070	XMM-077	no	…	yes	yes
LL14-072	01:33:34.99	30:29:54.6	18	2.5	…	LL14-072	XMM-076	yes	…	yes	yes
LL14-075	01:33:37.02	30:33:10.0	75	1.7	…	LL14-075	XMM-084	yes	…	yes	yes
LL14-079	01:33:38.65	31:02:38.8	60	6.8	…	LL14-079	XMM-087	no	…	yes	yes
LL14-080	01:33:39.59	30:34:26.0	62	1.4	…	LL14-080	XMM-088	yes	…	yes	yes
LL14-081	01:33:40.53	30:10:51.7	47	7.5	…	LL14-081	XMM-090	yes	…	yes	yes
LL14-092	01:33:47.52	30:17:13.8	57	6.0	…	LL14-092	XMM-103	no	…	yes	yes
LL14-093	01:33:47.82	30:18:02.1	95	5.8	…	LL14-093	XMM-104	no	…	no	…
LL14-094	01:33:48.13	30:17:25.9	19	5.9	…	LL14-094	XMM-105	no	…	no	…
LL14-096	01:33:48.92	30:33:05.2	40	1.7	…	LL14-096	…	no	…	no	…
LL14-103	01:33:52.56	30:28:38.4	40	3.0	…	LL14-103	XMM-115	no	…	yes	yes
LL14-106	01:33:54.69	30:18:51.0	73	5.8	…	LL14-106	XMM-117	yes	…	yes	yes
LL14-109	01:33:55.29	30:16:49.0	31	6.4	…	LL14-109	XMM-121	no	…	yes	no
LL14-114	01:33:57.41	31:00:55.8	61	5.6	…	LL14-114	XMM-126	no	…	yes	yes
LL14-120	01:33:59.15	30:32:42.1	39	2.3	…	LL14-120	XMM-133	no	…	yes	yes

Table 1
(Continued)

Source	R.A. (2000)	Decl. (2000)	Diameter (pc)	ρ (kpc)	L10	LL14	XMM	X-Ray Detected	Previous Spectrum	New Spectrum	[S II]:Hα Confirmed
LL14-122	01:34:00.25	30:39:28.9	40	0.8	…	LL14-122	XMM-137	yes	…	yes	yes
LL14-125	01:34:00.58	30:50:42.9	23	2.8	…	LL14-125	XMM-138	yes	…	yes	yes
LL14-128	01:34:02.10	30:28:34.5	37	3.5	…	LL14-128	XMM-141	no	…	yes	yes
LL14-133	01:34:04.88	30:58:30.7	73	4.8	…	LL14-133	XMM-146	no	…	yes	no
LL14-134	01:34:05.50	31:07:26.4	56	7.2	…	LL14-134	XMM-147	yes	…	yes	no
LL14-137	01:34:07.98	31:01:03.7	55	5.4	…	LL14-137	XMM-150	no	…	yes	yes
LL14-142	01:34:11.21	30:24:15.3	42	5.1	…	LL14-142	XMM-155	no	…	yes	yes
LL14-143	01:34:12.28	31:02:43.4	56	5.8	…	LL14-143	XMM-156	no	…	yes	no
LL14-144	01:34:12.90	30:23:24.3	47	5.5	…	LL14-144	XMM-158	no	…	yes	no
LL14-148	01:34:13.85	30:30:39.8	16	3.7	…	LL14-148	XMM-162	no	…	yes	no
LL14-153	01:34:14.55	30:44:36.2	52	2.0	…	LL14-153	XMM-167	no	…	yes	yes
LL14-162	01:34:19.45	30:52:48.9	76	3.5	…	LL14-162	XMM-176	yes	…	no	…
LL14-163	01:34:19.68	30:33:41.5	38	3.5	…	LL14-163	XMM-177	no	…	no	…
LL14-167	01:34:24.08	30:33:24.4	61	3.9	…	LL14-167	XMM-181	no	…	no	…
LL14-168	01:34:24.48	30:48:58.3	81	3.0	…	LL14-168	XMM-182	no	…	yes	yes
LL14-173	01:34:29.77	30:35:08.4	86	4.0	…	LL14-173	XMM-187	yes	…	yes	yes
LL14-174	01:34:30.25	30:56:36.2	34	4.5	…	LL14-174	…	no	…	no	…
LL14-180	01:34:37.40	30:44:11.0	62	3.7	…	LL14-180	XMM-194	no	…	yes	yes
LL14-182	01:34:39.69	30:39:17.6	65	4.3	…	LL14-182	XMM-196	no	…	yes	yes
LL14-183	01:34:39.94	31:06:02.7	54	6.8	…	LL14-183	XMM-197	no	…	yes	yes
LL14-187	01:34:42.68	30:40:51.5	39	4.4	…	LL14-187	XMM-202	no	…	yes	yes
LL14-188	01:34:44.02	31:01:48.9	81	6.0	…	LL14-188	XMM-203	no	…	yes	no
LL14-189	01:34:45.40	30:35:35.2	50	5.3	…	LL14-189	XMM-205	no	…	yes	yes
LL14-190	01:34:45.88	30:57:19.1	51	5.3	…	LL14-190	XMM-206	no	…	yes	yes
LL14-191	01:34:47.24	30:34:25.0	37	5.6	…	LL14-191	XMM-207	no	…	yes	no
LL14-192	01:34:50.48	31:07:38.6	56	7.3	…	LL14-192	XMM-208	no	…	no	…
LL14-193	01:34:52.48	30:50:22.2	85	5.0	…	LL14-193	XMM-209	no	…	yes	yes
LL14-195	01:34:58.60	31:10:09.4	44	8.1	…	LL14-195	XMM-212	no	…	no	…
LL14-196	01:34:59.19	30:40:16.5	36	5.9	…	LL14-196	XMM-213	no	…	yes	yes
LL14-198	01:35:00.40	31:02:36.3	73	6.8	…	LL14-198	XMM-215	no	…	yes	no
LL14-199	01:35:01.82	30:39:53.9	81	6.1	…	LL14-199	XMM-217	no	…	yes	yes

References. BK85 = Blair & Kirshner (1985); G98 = Gordon et al. (1998); L10 = Long et al. (2010); S93 = Smith et al. (1993).

(This table is available in machine-readable form.)

combined the spectra for various nights, weighting the spectra by exposure time on each night. In Figure 2, we show several of our SNR candidate spectra, selected to indicate the typical quality of the spectra and sky subtraction for objects with a range of brightness. For comparison, we also show one of our H II region spectra.

We extracted line fluxes for several important emission lines expected in SNRs: Hβ, [O III] $\lambda\lambda$4959, 5007, [O I] λ6300, Hα, [N II] $\lambda\lambda$6548, 6583, and [S II] $\lambda\lambda$6717, 6731, using the same Gaussian fitting routine we have used for extracting line fluxes from 1D spectra on other projects (e.g., M83; see Winkler et al. 2017). The results of these fits are summarized for the SNR candidates in Table 2. The columns in the table include the object name, the Hα flux[9] in units of 10^{-17} erg cm^{-2} s^{-1}, and the fluxes for other lines relative to Hα. For the doublets where the line ratio is constrained by atomic physics, we list only the stronger of the lines. For S II, where the ratio of the two lines in the doublet is density-sensitive, we list the ratio between the [S II]λ6717 and [S II]λ6731 lines, as well as their sum relative to Hα. We follow the convention where the Hα flux is taken to be 300, except for the ratio of the two [S II] lines, where we give the simple ratio between those two lines. We have not quoted errors for the various values contained in the table, as it is unclear how to do this in a robust manner. Based on a comparison of the flux ratios in spectra of the same object observed on multiple nights, the ratio errors for bright, well-observed lines are typically less than 15%. Lines where the accuracy of the line ratio is clearly worse than this have entries preceded by a ∼symbol.

Based on the tabulation provided by Long10, there are 85 SNRs in M33 that already had spectra; of these, we have new spectra of 77. A comparison of the [S II]:Hα ratios from earlier measurements to those from this paper is shown in Figure 3. Given the variety of instruments, the different slits and fibers used in the earlier estimates, and the fact that none of the apertures or fibers covered an entire SNR, there is quite good agreement between the past spectra and the new measurements.

There are eight objects for which historical spectra exist and for which we did not get new spectra: L10-017, L10-021, L10-047, L10-056, L10-083, L10-095, L10-102, and L10-129. In the earlier spectra, all of these objects have [S II]:Hα ratios >0.4, and thus they should be considered valid SNRs based on this criterion. As such, we have listed them as "[S II]:Hα Confirmed" in Table 1.

[9] This is the flux sampled by a 1.″5 diameter fiber, *not* the total flux from the entire object. Because all the objects are larger than the fibers that sampled them, this flux is best interpreted as a surface brightness.

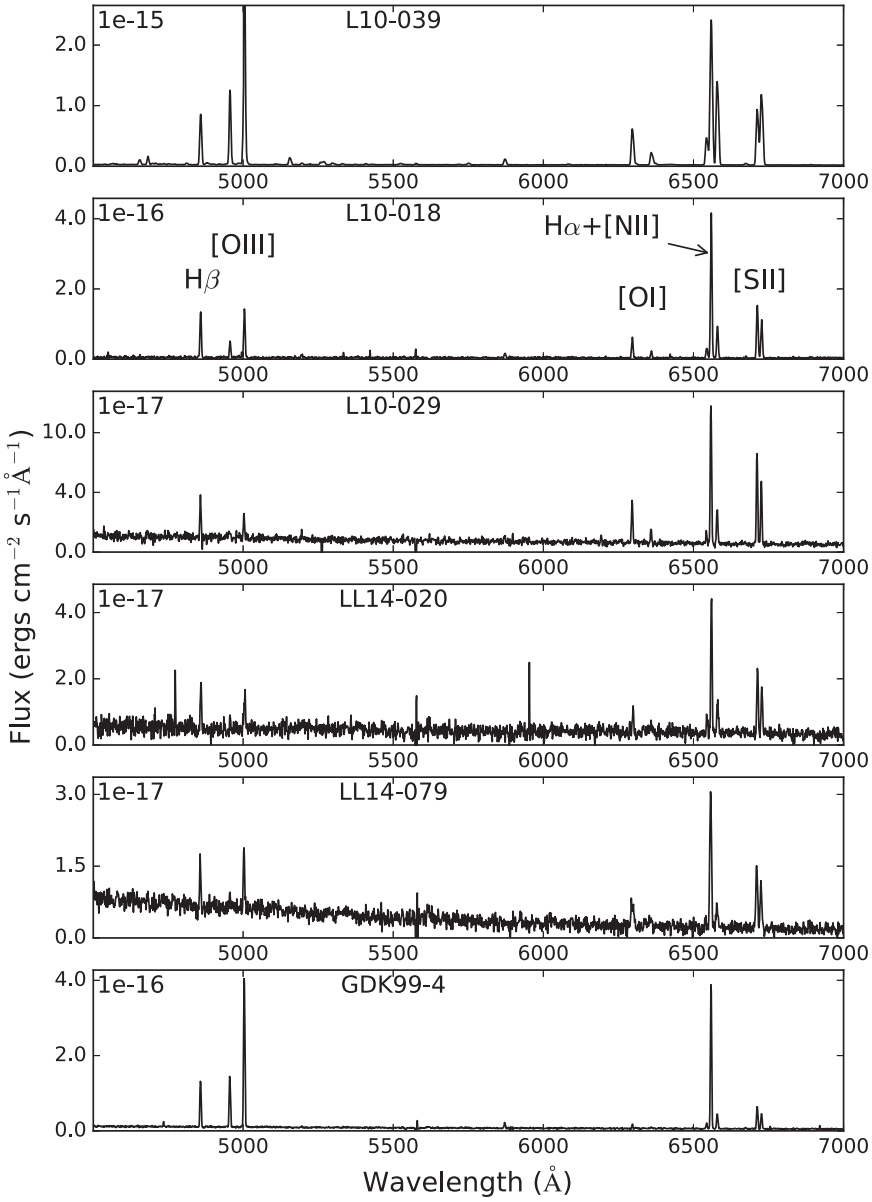

Figure 2. Example spectra. The spectra of five SNR candidates are shown in the upper five panels of the figure. The various spectra were selected to indicate the quality of the data as a function of surface brightness. The continuum in the spectrum of L14-079 arises from the fact that, in addition to emission from the nebula, the fiber captured light from stars along the line of sight as well. The spectrum of a moderately bright H II region is shown in the bottom panel, for comparison. The lines of interest are labeled in the second panel. The flux scaling numbers in the upper left corner of each panel should be applied to the values on the vertical axis of that panel.

3. Results

As noted in Section 1, the primary criterion used to discriminate optical SNRs from photoionized nebulae is that the ratio of [S II]:Hα be $\gtrsim$0.4. This criterion has been effectively applied for identifying objects in many galaxies. However, its reliability depends on a number of variables, including how low in surface brightness one surveys, how the metallicity varies, and various characteristics of the H II regions. At some stage, questions of size and morphology must also be taken into account. For brighter nebulae in most nearby galaxies, the [S II]:Hα criterion gives a clean separation between SNRs and H II regions. However, for some galaxies, and especially for low surface brightness objects, many nebulae have [S II]:Hα ratios in the range 0.2–0.5 that blur the dividing line between SNRs and H II regions. Of course, observational uncertainty also becomes increasingly significant for fainter objects, further obfuscating the demarcation.

Our original candidate sample comprised 217 sources, of which we obtained spectra for 197. The [S II]:Hα ratios for these 197 are plotted as a function of the measured Hα flux in Figure 4. Of these, 170 (86%) satisfy the [S II]:H$\alpha > 0.4$ criterion. Further breaking these down, 108 of the 110 SNR candidates that appear in *both* the Long10 and LL14 lists meet the criterion, as do 15 of 18 identified only by Long10, but only 47 of 69 of those identified only by LL14.

It is perhaps not surprising that a higher percentage of the LL14-only objects have lower ratios; these are systematically fainter than the other candidates. We have inspected many of the LL14 objects on the LGGS images, and while those of brightness comparable to the fainter Long10 objects look like reasonable candidates, many of the faintest LL14

Table 2
Emission Line Fluxes of SNR Candidates[a]

Source	Hα Flux[b]	Hβ	[O III] λ5007	[O I] λ6300	Hα	[N II] λ6584	[S II] λ6717	[S II] λ6731	[S II]:Hα	FWHM (Å)
L10-001	51	95	76	56	300	45	127	90	0.72	5.7
L10-002	168	95	274	47	300	51	109	77	0.62	5.0
L10-003	89	92	51	22	300	42	79	57	0.45	4.9
L10-004	46	88	∼36	∼62	300	34	129	89	0.73	5.2
L10-005	32	70	301	∼39	300	55	122	83	0.69	5.3
L10-006	28	116	257	∼26	300	64	91	65	0.52	5.3
L10-007	27	90	34	79	300	35	126	83	0.70	5.1
L10-008	92	94	30	∼25	300	55	112	79	0.64	5.4
L10-009	120	101	257	44	300	65	154	108	0.87	5.2
L10-010	55	91	55	50	300	53	125	93	0.73	5.3
L10-011	828	100	142	77	300	62	136	117	0.84	5.9
L10-012	377	95	74	18	300	58	110	78	0.63	5.0
L10-013	29	110	359	…	300	42	94	57	0.50	5.8
L10-014	339	97	72	26	300	59	114	81	0.65	5.0
L10-016	65	91	140	48	300	72	125	89	0.72	5.2
L10-018	252	93	95	41	300	68	115	84	0.66	5.7
L10-019	105	108	161	27	300	47	99	68	0.56	4.9
L10-020	33	73	262	∼50	300	83	159	115	0.91	5.0
L10-022	53	89	95	79	300	77	146	104	0.83	5.1
L10-023	110	88	198	59	300	73	100	86	0.62	5.7
L10-024	95	55	∼21	∼18	300	66	91	64	0.52	4.8
L10-025	313	89	221	∼17	300	51	63	61	0.41	6.0
L10-026	155	94	103	24	300	74	130	92	0.74	5.0
L10-027	93	81	∼27	62	300	76	163	113	0.92	5.1
L10-028	132	92	69	∼14	300	81	84	60	0.48	4.8
L10-029	65	83	42	88	300	75	196	132	1.09	5.1
L10-030	129	81	33	∼11	300	70	79	57	0.45	5.0
L10-031	100	90	227	68	300	103	183	136	1.06	5.8
L10-032	242	72	73	114	300	88	188	139	1.09	5.8
L10-033	30	∼89	…	∼81	300	62	167	109	0.92	5.1
L10-034	105	∼51	395	∼21	300	101	121	94	0.72	6.4
L10-035	108	…	…	…	300	…	67	43	0.37	5.5
L10-036	1850	87	133	106	300	139	173	168	1.14	8.3
L10-037	26	85	286	∼31	300	78	117	91	0.69	6.2
L10-038	72	99	84	…	300	69	107	75	0.61	4.8
L10-039	2342	83	326	76	300	178	117	155	0.91	9.1
L10-040	112	97	87	∼10	300	63	58	42	0.33	5.0
L10-041	35	∼54	∼44	81	300	88	187	138	1.08	5.0
L10-042	41	∼38	58	77	300	60	161	113	0.91	5.0
L10-043	128	95	44	∼20	300	84	105	71	0.58	4.8
L10-044	68	∼78	58	97	300	90	174	122	0.99	6.0
L10-045	2485	79	153	39	300	124	131	117	0.83	7.4
L10-046	77	∼89	68	67	300	99	171	126	0.99	5.7
L10-048	164	∼83	20	∼12	300	85	97	65	0.54	4.8
L10-049	86	∼64	186	∼46	300	134	148	103	0.83	5.0
L10-050	72	86	54	…	300	96	101	66	0.56	5.0
L10-051	13	56	∼65	…	300	54	146	110	0.85	5.0
L10-052	106	83	35	…	300	76	90	63	0.51	4.9
L10-053	220	81	59	28	300	51	102	74	0.58	5.4
L10-054	114	82	52	36	300	54	129	92	0.74	5.2
L10-055	168	83	13	∼17	300	87	119	85	0.68	4.8
L10-057	131	79	31	28	300	90	117	81	0.66	4.9
L10-058	112	93	13	∼29	300	86	126	91	0.73	4.9
L10-059	60	∼28	75	∼47	300	173	194	140	1.11	5.2
L10-060	305	72	59	56	300	127	143	102	0.82	5.2
L10-061	217	85	30	55	300	101	162	114	0.92	4.9
L10-062	31	67	∼21	…	300	90	114	92	0.68	4.8
L10-063	20	∼66	∼54	∼53	300	101	152	110	0.87	4.9
L10-064	41	∼60	242	…	300	101	129	90	0.73	5.5
L10-065	146	82	32	∼25	300	108	119	83	0.67	4.9
L10-066	21	64	∼52	∼86	300	111	207	145	1.17	5.1
L10-067	61	81	69	∼49	300	91	143	101	0.81	5.1
L10-068	52	97	294	60	300	87	158	107	0.89	4.8

Table 2
(Continued)

Source	Hα Flux[b]	Hβ	[O III] λ5007	[O I] λ6300	Hα	[N II] λ6584	[S II] λ6717	[S II] λ6731	[S II]:Hα	FWHM (Å)
L10-069	142	∼71	38	∼33	300	88	142	101	0.81	5.1
L10-070	416	90	74	57	300	117	164	119	0.94	5.3
L10-071	1113	94	194	86	300	130	172	155	1.09	7.4
L10-072	54	∼31	93	∼60	300	190	206	152	1.19	4.9
L10-073	65	94	119	∼35	300	70	144	97	0.80	5.1
L10-074	151	79	49	87	300	102	191	133	1.08	5.7
L10-075	43	∼47	∼26	74	300	132	206	133	1.13	4.9
L10-076	180	90	107	34	300	114	124	87	0.70	4.8
L10-077	258	88	17	∼8	300	67	78	53	0.44	4.8
L10-078	295	88	160	93	300	161	206	152	1.19	5.5
L10-079	148	90	14	∼20	300	74	102	70	0.57	4.9
L10-080	175	62	123	95	300	159	198	159	1.19	5.5
L10-081	77	∼66	164	…	300	89	111	82	0.64	4.8
L10-082	33	∼65	303	∼41	300	95	180	123	1.01	6.2
L10-084	55	∼61	409	∼39	300	178	214	148	1.20	9.0
L10-085	138	73	223	82	300	136	188	146	1.11	5.3
L10-086	48	71	85	∼69	300	90	95	96	0.64	5.1
L10-087	41	65	75	…	300	87	137	106	0.81	5.0
L10-088	30	67	113	∼59	300	102	170	131	1.00	5.1
L10-089	144	83	35	∼18	300	84	102	74	0.59	4.8
L10-090	19	∼51	505	…	300	139	191	133	1.08	5.9
L10-091	27	86	346	∼48	300	126	199	138	1.12	5.7
L10-092	79	81	100	42	300	106	143	99	0.81	4.9
L10-093	21	∼19	173	∼68	300	103	174	121	0.98	4.9
L10-094	96	∼75	344	∼14	300	110	131	102	0.78	5.1
L10-096	987	90	51	148	300	118	235	195	1.43	5.5
L10-097	96	80	159	61	300	118	153	117	0.90	5.6
L10-098	94	88	106	∼15	300	62	76	53	0.43	4.8
L10-099	155	85	30	27	300	90	145	105	0.83	4.9
L10-100	37	69	292	…	300	98	152	106	0.86	5.8
L10-101	240	94	18	25	300	90	151	105	0.85	4.9
L10-103	26	62	182	…	300	119	160	111	0.90	5.4
L10-104	45	∼73	46	∼80	300	101	172	132	1.01	5.5
L10-105	57	82	131	62	300	83	171	121	0.97	5.8
L10-106	17	∼70	249	∼91	300	104	175	119	0.98	4.8
L10-107	66	85	247	∼34	300	93	141	100	0.80	6.0
L10-108	60	95	98	∼14	300	61	95	71	0.55	4.9
L10-109	389	92	225	10	300	60	68	48	0.39	5.0
L10-110	151	96	43	26	300	59	101	71	0.57	5.0
L10-111	55	74	183	∼47	300	120	172	116	0.96	7.7
L10-112	19	∼43	51	…	300	100	191	144	1.11	4.5
L10-113	183	85	284	∼15	300	55	82	57	0.46	5.0
L10-114	391	98	316	40	300	72	124	89	0.71	5.1
L10-115	38	99	90	69	300	62	140	96	0.79	5.9
L10-116	18	∼71	239	…	300	93	162	113	0.92	4.7
L10-117	45	91	81	∼58	300	73	146	100	0.82	6.1
L10-118	30	∼70	∼67	…	300	64	122	94	0.72	5.5
L10-119	18	81	∼54	…	300	63	81	57	0.46	4.9
L10-120	113	100	376	22	300	97	102	70	0.57	4.9
L10-121	28	70	295	…	300	52	75	46	0.40	7.1
L10-122	102	94	275	37	300	80	162	118	0.93	5.1
L10-123	56	90	86	106	300	77	188	132	1.06	5.6
L10-124	1527	92	112	42	300	68	107	86	0.64	5.4
L10-125	80	97	280	54	300	102	165	118	0.94	5.3
L10-126	62	100	693	∼49	300	110	106	71	0.59	4.8
L10-127	61	87	…	∼24	300	52	102	73	0.58	4.9
L10-128	233	97	151	32	300	82	131	90	0.74	5.7
L10-130	85	95	203	∼37	300	85	152	103	0.85	5.3
L10-131	38	115	254	…	300	52	73	49	0.41	4.9
L10-132	134	87	14	…	300	40	45	32	0.26	4.8
L10-133	116	96	33	∼13	300	52	96	67	0.54	4.9
L10-134	18	100	153	∼58	300	57	125	80	0.68	5.0
L10-135	32	95	∼55	…	300	63	119	83	0.67	5.0

Table 2
(Continued)

Source	Hα Flux[b]	Hβ	[O III] λ5007	[O I] λ6300	Hα	[N II] λ6584	[S II] λ6717	[S II] λ6731	[S II]:Hα	FWHM (Å)
L10-136	53	107	45	…	300	52	63	44	0.36	4.9
L10-137	40	95	∼40	∼39	300	34	126	83	0.69	5.1
LL14-001	18	113	…	…	300	29	95	78	0.58	4.8
LL14-002	17	92	138	∼49	300	35	115	79	0.65	5.2
LL14-004	37	104	59	…	300	30	∼37	∼22	∼0.20	4.8
LL14-005	8	119	621	…	300	36	65	47	0.37	4.6
LL14-006	15	∼79	…	∼48	300	50	109	74	0.61	5.0
LL14-007	19	90	…	…	300	30	∼53	∼22	∼0.25	5.0
LL14-008	10	∼76	…	…	300	39	∼51	∼30	∼0.27	4.6
LL14-009	23	98	114	…	300	29	41	27	0.22	4.7
LL14-010	19	∼77	…	…	300	39	88	53	0.47	5.1
LL14-012	24	107	…	…	300	43	67	44	0.37	4.8
LL14-014	4	∼83	402	…	300	−8	∼89	∼30	∼0.40	4.6
LL14-016	35	88	…	…	300	44	74	56	0.43	4.9
LL14-020	23	96	83	∼50	300	73	153	107	0.87	5.1
LL14-023	44	90	∼29	∼33	300	40	66	43	0.36	4.9
LL14-030	19	108	415	…	300	35	81	64	0.48	5.9
LL14-032	6	…	…	…	300	…	…	…	…	5.5
LL14-038	17	86	136	…	300	82	126	93	0.73	5.1
LL14-040	8	…	…	∼151	300	84	133	90	0.74	4.9
LL14-043	21	88	117	…	300	63	128	87	0.72	5.0
LL14-044	26	44	…	…	300	54	78	52	0.43	4.6
LL14-046	5	∼126	…	…	300	12	∼82	∼38	∼0.40	4.5
LL14-047	48	82	427	…	300	51	69	52	0.40	4.7
LL14-048	18	…	…	…	300	∼16	∼35	∼33	∼0.23	6.2
LL14-049	56	91	∼46	…	300	54	73	49	0.41	4.9
LL14-051	60	85	…	…	300	51	92	65	0.52	4.8
LL14-054	18	∼58	…	…	300	78	102	58	0.53	4.6
LL14-055	4	…	∼484	…	300	∼136	253	173	1.42	4.7
LL14-057	28	59	∼18	…	300	49	57	38	0.31	4.6
LL14-058	15	70	405	∼93	300	64	131	108	0.80	5.9
LL14-059	9	97	…	…	300	∼40	46	64	0.37	4.7
LL14-063	2	…	∼288	…	300	…	∼102	∼146	∼0.83	6.2
LL14-065	11	∼71	…	…	300	∼45	149	91	0.80	4.6
LL14-070	10	∼29	…	∼124	300	35	∼116	∼56	∼0.58	5.0
LL14-072	250	90	239	55	300	96	170	126	0.99	5.8
LL14-075	68	77	70	…	300	81	123	70	0.64	5.1
LL14-079	21	78	98	∼80	300	51	135	93	0.76	6.9
LL14-080	37	…	109	…	300	96	130	93	0.75	4.7
LL14-081	33	82	68	79	300	37	107	76	0.61	5.1
LL14-092	11	∼38	501	…	300	40	∼82	∼46	∼0.43	4.5
LL14-103	25	72	…	…	300	65	86	62	0.49	4.9
LL14-106	17	90	104	…	300	52	122	85	0.69	6.3
LL14-109	13	88	…	…	300	40	43	30	0.25	4.9
LL14-114	14	97	…	…	300	13	83	47	0.43	5.0
LL14-120	87	89	69	…	300	81	110	76	0.62	4.8
LL14-122	50	∼41	91	…	300	136	121	86	0.69	4.7
LL14-125	20	66	184	…	300	95	179	119	0.99	5.1
LL14-128	9	∼55	…	…	300	63	111	90	0.67	4.6
LL14-133	16	71	∼54	…	300	14	28	19	0.15	4.8
LL14-134	5	∼79	∼177	…	300	…	…	…	…	4.2
LL14-137	22	104	…	…	300	42	91	61	0.50	5.7
LL14-142	11	85	…	…	300	50	81	53	0.45	4.7
LL14-143	12	…	…	…	300	∼23	46	29	0.25	5.2
LL14-144	13	∼113	…	…	300	∼34	∼63	∼45	∼0.36	4.7
LL14-148	59	82	495	…	300	58	59	45	0.35	4.8
LL14-153	22	55	106	…	300	89	112	78	0.63	5.1
LL14-168	22	63	∼33	…	300	62	87	64	0.50	4.9
LL14-173	7	∼59	…	…	300	∼78	∼96	∼79	∼0.58	4.5
LL14-180	37	84	37	…	300	52	79	55	0.44	4.9
LL14-182	13	63	…	…	300	∼31	103	64	0.56	5.2
LL14-183	11	88	…	…	300	36	113	78	0.64	6.0
LL14-187	27	88	…	…	300	42	75	51	0.42	4.9

Table 2
(Continued)

Source	Hα Flux[b]	Hβ	[O III] λ5007	[O I] λ6300	Hα	[N II] λ6584	[S II] λ6717	[S II] λ6731	[S II]:Hα	FWHM (Å)
LL14-188	8	∼71	…	…	300	…	…	…	…	4.7
LL14-189	8	88	218	…	300	70	175	95	0.90	5.1
LL14-190	3	…	547	…	300	…	…	…	…	5.3
LL14-191	21	79	…	∼71	300	49	58	38	0.32	5.0
LL14-193	3	…	∼262	…	300	…	165	165	1.10	4.2
LL14-196	31	103	134	49	300	53	132	93	0.75	5.3
LL14-198	10	…	∼83	…	300	∼22	∼38	∼20	∼0.19	4.6
LL14-199	11	116	…	…	300	42	105	77	0.61	5.1

Notes.
[a] Emission line strengths are listed relative to Hα set to 300.
[b] Hα Flux is in erg cm^{-2} s^{-1} in the 1.″5 diameter fiber of HectoSpec.

(This table is available in machine-readable form.)

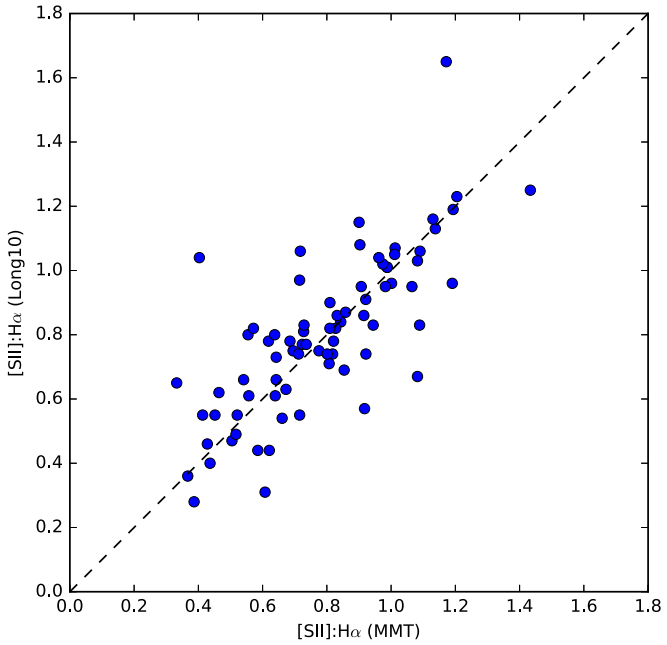

Figure 3. The [S II]:Hα ratio of SNRs measured from spectra obtained here with the MMT, compared to [S II]:Hα ratios from spectra of SNRs collated by Long10. Ideally, all the points would fall along the dashed 1:1 line. Given the the variety of instrumental setups involved, the agreement is probably as good as one could reasonably expect.

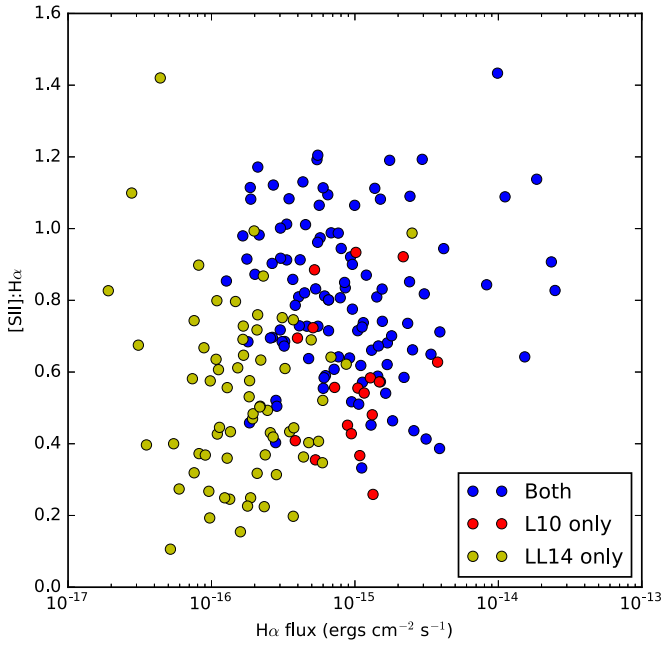

Figure 4. The [S II]:Hα ratio of SNRs measured from spectra obtained with the MMT as a function of the Hα flux obtained from the spectra. The SNR candidates that appear in both Long10 and LL14 are plotted in blue, those from only Long10 in red, and those from only LL14 in yellow. The LL14-only candidates are generally fainter than the others, and have a higher dispersion in the [S II]:Hα ratio.

objects are exceedingly faint in Hα and barely visible at all in [S II]. Now that we have spectra of many of these objects, we find that a number have low [S II]:Hα ratios, even given the uncertainties that attend the relatively low signal-to-noise spectra. Our spectra, together with their morphology on LGGS images, lead us to reject the following LL14 objects as bona fide SNR candidates going forward: LL14-004, 009, 014, 032, 046, 048, 057, 059, 109, 133, 134, 188, and 198. Several additional objects should be considered marginal SNR candidates at best, given our assessment of M33 H II regions in the next section, as well as the observational uncertainties in their determined ratios. However, we retain all the remaining Long10 and LL14 SNR candidates in the color-coded plots (such as Figure 8) presented below.

In addition to measuring the line fluxes for the objects in our sample, we also measured the line widths (full width at half maximum; FWHM). In fitting the lines, we fit a single width to closely spaced line complexes, viz., a single FWHM for Hβ and [O III], one for Hα and [N II], and one for the [S II] doublet. A comparison of the velocity widths for all three complexes shows very similar results; hence, we concentrate on the Hα–[N II] fits, where the signal-to-noise is highest. In Figure 5, we show the FWHM for both SNRs and H II regions, plotted as a function of Hα flux. For the H II regions, the fits are tightly clustered about the mean width of 5.43 Å with an rms dispersion of only 0.06 Å. However, the FWHM distribution for the SNRs has a mean of 5.85 Å with dispersion 0.78 Å. As expected, the dispersion is larger for fainter objects with lower S/N, but it is clear that the FWHM distribution for the SNRs skews to higher than instrumental values.

One would expect the material in H II regions to be simply that of the ambient ISM. Hence, their emission line widths should be essentially the instrumental value. For SNRs, the

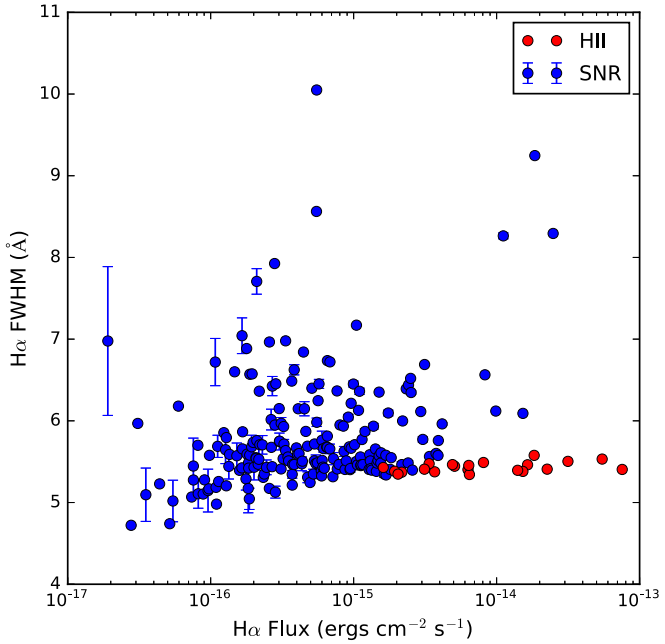

Figure 5. In fitting the lines, we fit a single FWHM for the three lines in the Hα + [N II] complex. The figure shows the FWHM for the line complex as a function of Hα flux. The FWHM for H II regions all cluster around 5.4, whereas the SNRs have a broader distribution that is asymmetric toward higher values. The formal errors for a subsample of the values are shown. Plots made with the [S II] line complex are very similar.

lines will be Doppler broadened with a velocity characteristic of their shock velocity.[10] If one assumes that the observed resolution

$$\mathrm{FWHM_{obs}} = \sqrt{\mathrm{FWHM_{inst}^2} + \mathrm{FWHM_{SNR}^2}}\,, \qquad (1)$$

then at Hα, a width of 5.85 Å corresponds to velocity broadening of 100 km s^{-1}, typical of older SNRs. A FWHM of 7 Å corresponds to 200 km s^{-1}, and 10 Å would correspond to 380 km s^{-1}, neither of which is unusual for radiative shocks. However, to the extent that we have chosen the brightest sections of the SNR to observe, we have chosen limb-brightened regions that are seen edge-on, biasing the FWHM to values below the shock speed. We have found no obvious correlations between the FWHM and other properties of the SNRs, such as diameter. In particular, we find *no* objects with velocities approaching 1000 km s^{-1} or more, such as one finds in young, ejecta-dominated SNRs like Cas A (Milisavljevic et al. 2012). Furthermore, we see no evidence for wildly discrepant chemical abundances as seen in ejecta-dominated SNRs. While this is perhaps not surprising for a sample assembled based on the [S II]:Hα ratio, we also examined the LGGS [O III] images in Long10 and were not able to identify any oxygen-rich candidate SNRs.

[10] The thermal broadening for H is only about 20 km s^{-1}, too low to be measured at our spectral resolution. For heavier elements, the thermal broadening is considerably less. However, because the bulk velocity of material behind a radiative shock is very close to that of the shock, and a typical line of sight through the SNR includes multiple regions on both sides of the SNR, the observed line broadening should be of the same order as the shock speed in the denser gas encountered by the SNR shock. Because optical radiation in most SNRs arises from radiative secondary shocks propagating into denser gas, the observed broadening will be less than that of the primary SNR shock.

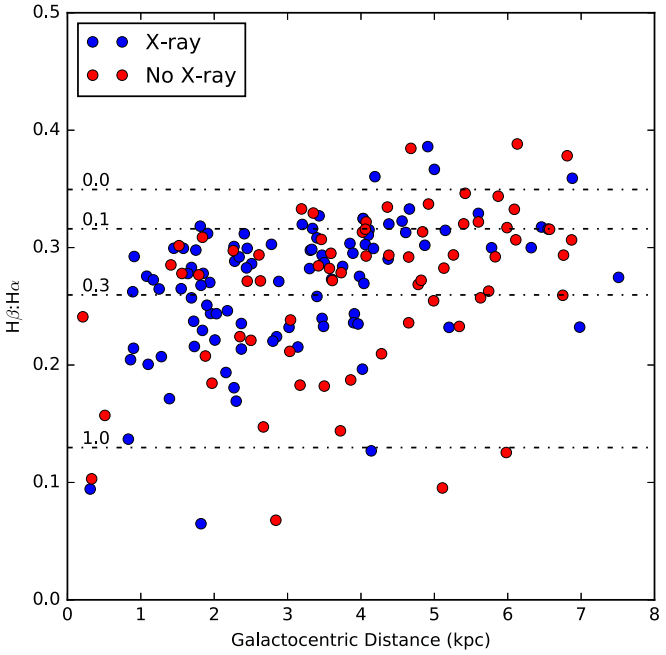

Figure 6. The Hβ:Hα flux ratio as a function of galactocentric distance. The dashed lines indicate reddening values (from top to bottom) of $E(B-V) =$ 0.0, 0.1, 0.3, and 1.0.

3.1. Reddening

The intrinsic value of Hβ:Hα at low optical depth is constrained by the physics of recombination to be 0.35 (e.g., Osterbrock & Ferland 2006), but absorption due to—or more correctly, scattering by—dust grains along the line of sight leads to lower observed ratios. The observed Hβ:Hα ratio for the SNR sample for which we have spectra is shown in Figure 6, as a function of GCD. A very similar figure could have been made for the Lin17 H II regions. There is a large variation in Hβ:Hα that reflects, at least in part, the location of candidates above or below the galactic plane of M33, as well as local variations in the amount of dust. There is also an overall trend of decreasing absorption with larger GCD, due to the generally lower density (for both gas and dust) farther from the center of the galaxy. The X-ray-detected SNRs do not exhibit significantly less reddening than the non-X-ray-detected ones, presumably because the overall reddening is still fairly low. A reddening of $E(B-V) \approx 0.3$, typical of the value seen in the inner part of the galaxy, corresponds to an effective hydrogen column density of 1.7×10^{21} cm^{-2}.

3.2. Density Effects

The ratio of [S II] 6717:6731 is a well-known density diagnostic, driven by the importance of collisional excitation/de-excitation of the upper levels (e.g., Osterbrock & Ferland 2006). This line ratio is presented in Figure 7 for the 170 SNR candidates with an [S II]:Hα ratio greater than 0.4, plotted as a function of SNR diameter (left panel) and flux through the 1.″5 fibers (right panel). The 112 candidates with X-ray detections are plotted separately from those without X-rays. The ratios for most of the objects indicate that optical emission arises from material with density $n < 100$ cm^{-3}. The left panel of the figure shows that, at diameters $\lesssim$40 pc, the fraction of SNRs detected in X-rays and the fraction with higher density are both greater than for SNRs with larger diameter. The right panel

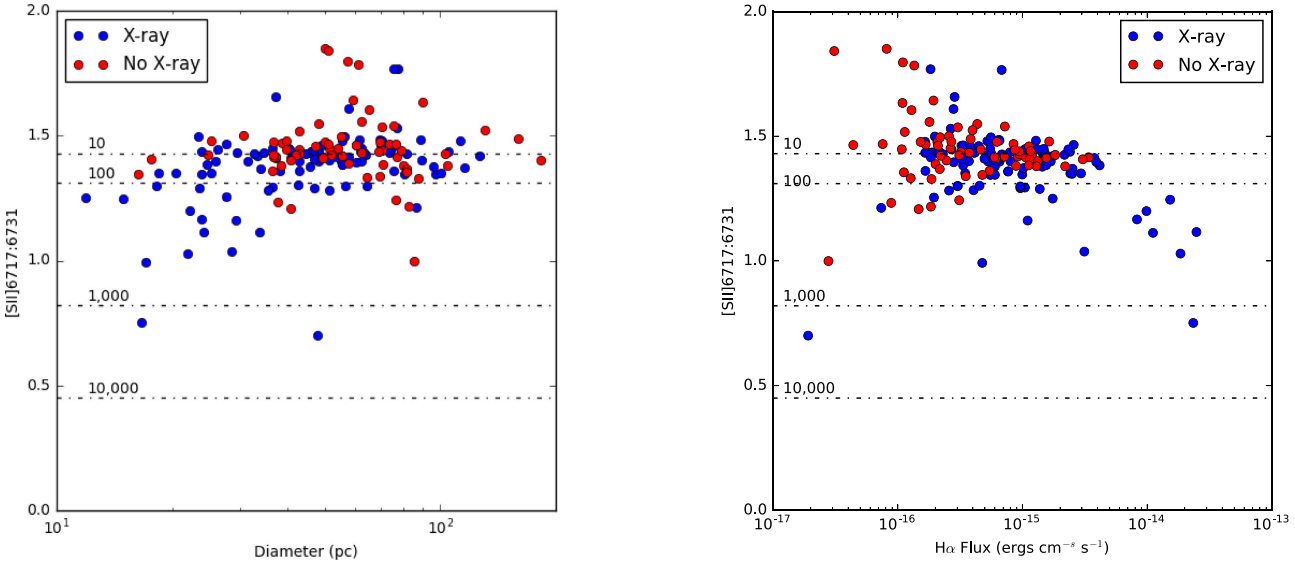

Figure 7. The density-sensitive line ratio [S II] λ6717:[S II] λ6731 plotted as a function of SNR diameter (left panel) and flux (right panel), as measured through a 1.″5 diameter fiber. Only objects with [S II]:Hα greater than 0.4 have been plotted. Objects with and without X-ray detections are plotted separately. The dashed lines indicate electron densities of 10, 100, 1000, and 10,000 cm^{-3} from top to bottom, respectively (Osterbrock & Ferland 2006). Most SNRs have ratios near the low-density limit. Those that show higher densities lie preferentially at smaller diameters and higher flux levels.

shows that, with considerable scatter, SNRs with higher flux tend to be detected in X-rays and also to show higher densities. The trends with diameter are also seen for SNRs in M83 (Winkler et al. 2017). The Hα emission per unit area of a shock is proportional to the pre-shock density, and it increases with shock speed at a rate between V_s and V_s^2. The density in the region that emits [S II] increases with the ram pressure, $n_0 V_s^2$, though the relation is complicated by the contribution of magnetic pressure. Therefore, one would expect the density derived from [S II] to increase with the Hα flux, and that is borne out in the figure. It is not entirely clear which of the two effects, density or shock velocity, dominates, though the absence of any truly high-velocity SNRs and the fact that soft X-ray emissivity (and hence detectability) peaks just as SNRs are entering the radiative phase favors density as the primary cause. On the other hand, if one compares the ratio of [S II] 6717:6731 for candidates with [S II]:Hα greater than 0.4 and measured line widths less or greater than 5.85 Å (corresponding to velocity width of 100 km s^{-1}), one finds the [S II] 6717:6731 ratio to be 1.42 $\pm$ 0.13 for the "narrow line" objects' and 1.28 $\pm$ 0.23 for the "broad line" objects, suggesting that shock velocity does play a role. This is an area where systematic studies at higher spectral resolution of a large number of SNRs in a galaxy like M33 would help.

4. Discussion

4.1. Confirming Bona Fide SNRs: Validity of the [S II]:Hα Ratio

There are important caveats when using the [S II]:Hα ratio to distinguish H II regions from SNRs. Perhaps most significant is that not all photoionized gas displays a low [S II]:Hα ratio at faint surface brightness. Diffuse ionized gas (DIG) is known to be photoionized and yet can have a high [S II]:Hα ratio, due to the low density of the gas and its relatively far distance from the ionizing sources (Reynolds 1985; Wood et al. 2010). The same effect is seen on the rims of large H II complexes, which often have regions with an elevated [S II]:Hα ratio compared to the interior. Blair & Long (1997) encountered this situation when investigating the Sculptor group spirals NGC 300 and NGC 7793, where the [S II]:Hα criterion broke down as a clean diagnostic. Furthermore, at ground-based spatial resolution, a diffuse patch of DIG may not be clearly distinguishable from a faint SNR, so a morphology criterion does not necessarily clarify the object identifications. Many of the SNRs and candidates in M33 have substantially lower surface brightness than the prominent H II regions (Figure 8, left). Thus, confusion near the [S II]:Hα = 0.4 criterion (or any particular fixed value) used to separate H II regions from SNRs can be a concern, especially for fainter objects.

Fortunately, Lin17 have recently conducted an extensive spectroscopic survey of H II regions in M33 using instrumentation identical to our own study. We can use their results to investigate the full range of observed ratios in a broad sample of emission regions, without being limited to the brightest H II regions that have typically been observed previously. Lin17 reported spectra of 413 positions in M33, distributed over a large range of surface brightness and GCD. Starting from a fairly low-resolution star-subtracted Hα image of M33 (taken from the 0.6 m Burrell Schmidt telescope, with a resolution of $\sim$4″, as described by Hoopes et al. 2001), they selected fiber positions quasi-automatically by using an algorithm that identified extended peaks of Hα emission. To avoid confusion with poorly subtracted stars, Lin17 avoided positions coincident with cataloged 2MASS sources,[11] but they appear not to have applied any other criteria to their target selection. Consequently, a number of the Long10 and LL14 SNR candidates were incidentally included in their survey. We used the Lin17 positions to create a region file that we overlaid on M33 images from the LGGS. Through visual inspection of the images with Long10 and LL14 candidates also outlined, we eliminated 35 of the Lin17 spectra that were actually coincident with or overlapped SNR candidates.

[11] Nevertheless, a number of Lin et al. (2017) spectra still include optically bright stars.

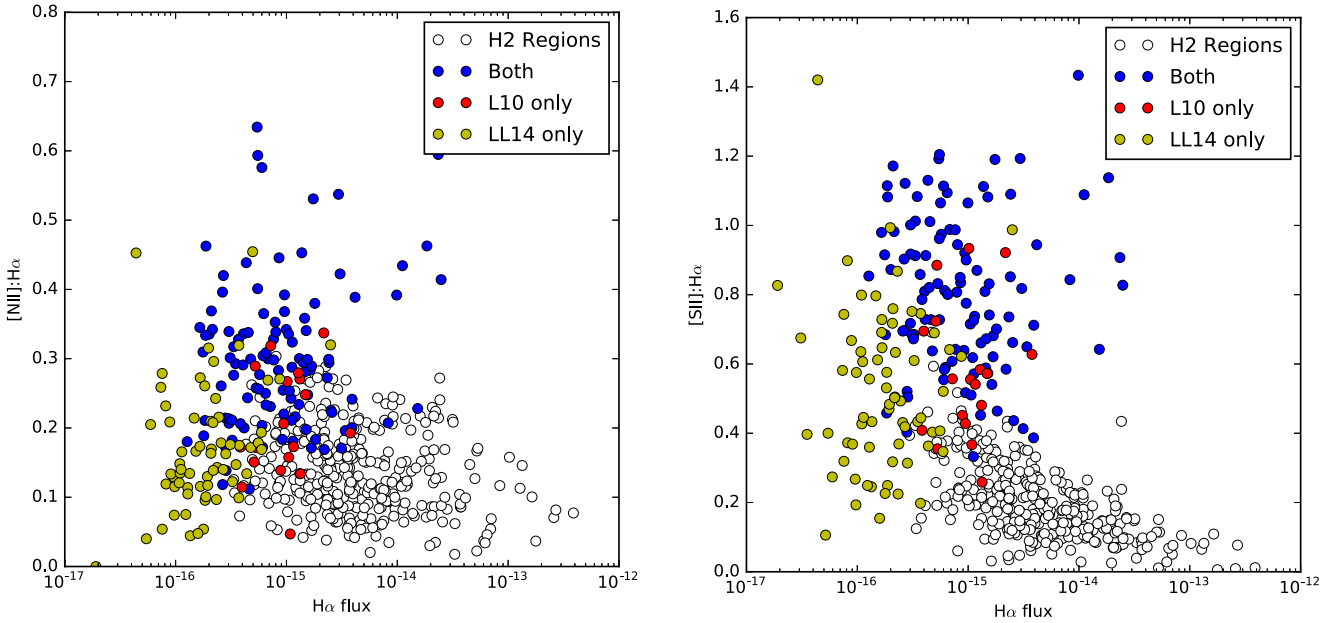

Figure 8. Comparison of the [N II]:Hα (left) and [S II]:Hα (right) ratios of SNR candidates to the Lin17 H II regions, after pruning the Lin sample as discussed in the text. The SNR sample is split into objects reported in both L10 and LL14, those in L10 only, and those in LL14 only. The ratios are plotted as a function of Hα flux, which is essentially a surface brightness through the filled Hectospec fibers.

In reviewing the other Lin17 fiber positions on the star-subtracted Hα images, we elected to eliminate spectra where the Lin17 algorithm had placed fibers on faint arcs or rims of very large, diffuse structures, or where there were multiple fibers placed on a single large diffuse nebula. We also eliminated a few fiber positions that appeared to lie on regions where no clearly defined structure appeared to be present in the LGGS images. This resulted in the removal of another 38 fiber positions from consideration.

The Lin17 fiber positions (not including the 73 rejected) sample a diverse set of emission nebulae when projected on the LGGS images, which have higher spatial resolution than those used by Lin17. Some are on bright, well-defined regions; some are on bright regions, but displaced from the peak emission; others are at various locations in large H II region complexes; while still others are located on faint, diffuse patches that are nevertheless discernible on LGGS images. We suspect that some of the latter could be DIG, but have adopted the entire remaining set of 340 spectra as our "H II region" comparison sample in the figures that follow.

In Figure 8, we show the [S II]:Hα ratios for our sample of SNR candidates, along with the pared-down Lin17 sample of H II regions, as a function of the Hα flux as observed through the 1.″5 Hectospec fibers. For $F_{\rm H\alpha} \gtrsim 2 \times 10^{-15}$ erg cm^{-2} s^{-1}, there is a relatively clean separation between the SNRs and H II regions. As seen in many previous studies, all of these brighter SNR candidates have [S II]:H$\alpha > 0.4$, while the ratio is significantly lower for almost all of the brighter H II regions. At $F_{\rm H\alpha} \sim 10^{-15}$ erg cm^{-2} s^{-1} and below, however, the distinction becomes increasingly blurred. In general, these fainter "objects" (in both samples) are less well-defined than the brighter ones. Even if they are distinct objects, instrumental effects—such as the difficulty in subtracting truly diffuse Hα emission that may overlie the object, and lower signal-to-noise in the spectra—contribute to the dispersion in observed [S II]:Hα ratios for these faint objects.

Ambiguity between SNRs and H II regions can, to some degree, be attributed to advancing technology. Early studies of M33 (e.g., D'Odorico et al. 1978; Blair & Kirshner 1985), as well as elsewhere (e.g., Levenson et al. 1995), found clear distinctions based on the [S II]:Hα ratio. However, these studies were limited to the brightest and best-defined objects. Subsequent imaging and spectroscopy of increased depth and sensitivity have led to vastly larger samples that encompass objects that are (sometimes over) an order of magnitude fainter than previously achievable. Consequently, inclusion of fainter objects has also led to many for which the identification as photoionized versus shock-heated is less clear without confirmation from other criteria, such as radio or X-ray emission or secondary indicators in the optical spectra.

The MMT data for M33 clearly indicate that the set of bright objects with high [S II]:Hα ratios are fairly distinct from the bright H II region population; the long-standing comparison of such spectra with predictions from shock models provides strong evidence for shock heating. However, at lower surface brightnesses, the two distributions begin to merge. Hence, we should expect that there is some contamination of the SNR candidate catalog by H II regions, and it is equally likely that the SNR candidate list may be incomplete at these fainter levels.

Along these lines, about half of the LL14-only candidates in Figure 8 with [S II]:Hα ratio <0.4 and low Hα flux are unlikely to be SNR candidates, based on their morphology. These objects appear to form an extension of the H II region points to even lower surface brightnesses. However, a number of the LL14-only objects, including some of the faintest, clearly have elevated [S II]:Hα ratios consistent with their being shock-heated. Such confusion is not limited to LL14-only candidates. Fainter Long10 candidates are potentially uncertain as well, with ratio values that overlap those of the H II region sample at comparable flux.

4.2. Other Optical Diagnostics

In principle, secondary criteria such as object morphology in the imagery or other supporting line ratios could be considered

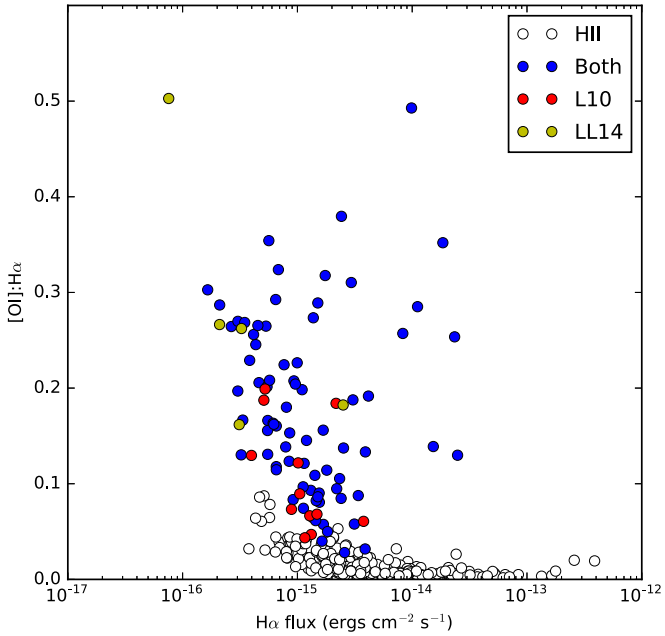

Figure 9. Comparison of the [O I]:Hα ratios of SNR candidates to the Lin17 H II regions (after pruning the Lin sample as discussed in the text), as a function of Hα flux. The SNR sample is split into objects reported in both L10 and LL14, those in L10 only, and those in L14 only.

for uncertain objects, in an attempt to clarify their nature. In developing the sample for Long10 for example, we required spatially extended candidates to show clear evidence of at least a partial shell structure in the LGGS images.

Among additional emission line ratios, the [O I] λ6300:Hα ratio is a possible criterion—and in certain cases, it may be a useful discriminant. Shock-heated gas often shows elevated [O I] emission in its cooling tail, just as it shows elevated [S II], and it is not normally observed in even low-ionization photoionized regions because the normal UV background in the ISM can keep it ionized. Observationally, measuring the [O I] lines spectroscopically is complicated for objects in galaxies with near zero red (or blue) shift, because of the difficulty in subtracting night sky emission. In our recent study of SNRs in M83 (Winkler et al. 2017), the redshift of 513 km s^{-1} was sufficient to allow us to measure [O I] emission in 110 of 118 SNR candidates. Resolving [O I] emission lines in M33, with a blueshift of 179 km s^{-1}, from the night sky lines is more challenging. Nevertheless, we have measured clear [O I] emission in the spectra of 93 of the 197 SNR candidates for which we have spectra. Detection of [O I] emission separate from the night sky is most difficult for the faintest objects with low signal-to-noise, which unfortunately is where it would be most valuable as a discriminant for the confused objects.

In Figure 9, we show the [O I]:Hα ratio for those objects where we were able to obtain reliable fits to the spectra, as well as for all of the pruned sample of Lin17 objects for which they give [O I] fluxes. [O I] is generally far stronger for SNRs than for H II regions, but there are a few SNRs for which [O I]:H$\alpha \lesssim 0.05$, as well as a few H II regions with higher ratios. As expected, this is especially true at low surface brightness. As with the [S II]:Hα ratio, SNRs generally have significantly higher values than H II regions, but there is no bright line that can cleanly separate the two classes of objects. Hence, rather than try to make a determination of object type for the objects at the lowest surface brightnesses, we simply point out the confusion. At low surface brightness in particular, it is especially important to obtain confirming information from another wavelength band before declaring an SNR candidate to be a bona fide SNR.

Another possible criterion for distinguishing SNRs from H II regions is the velocity broadening of the emission lines. Lin17 do not give linewidths for their large sample of H II regions, but as noted in Section 3, the 23 bright H II regions that we observed all have line widths that are consistent with that of the Hectospec instrument configuration. Our SNR candidates have line widths that are measurably greater in many cases, but in the fainter ones, the spectral resolution and S/N are not high enough to measure the broadening from SNR shocks with velocity $\lesssim$100 km s^{-1}, as are found in most old SNRs.

Much as we might like to identify a "gold standard" sample of SNRs identified based on their optical properties alone, we have not done this because it would undoubtedly exclude many actual SNRs (especially fainter ones).

4.3. X-Ray and Radio Diagnostics

At X-ray wavelengths, SNRs are extended sources with soft (line-dominated) X-ray spectra, compared to most X-ray binaries of comparable luminosity (and the many background AGN that contaminate X-ray catalogs of nearby galaxies). H II regions are also extended X-ray sources, but they are, with the exception of a few giant H II regions such as NGC 604 in M33 (Tüllmann et al. 2008), much fainter than SNRs. Because M33 is smaller in angular size than M31, is less inclined, and has less foreground absorption, M33 is perhaps the best-studied spiral galaxy at X-ray wavelengths. Very sensitive X-ray surveys of M33 have been made both with *Chandra* (Tüllmann et al. 2011) and *XMM-Newton* (Williams et al. 2015; Garofali et al. 2017). *Chandra*'s exquisite X-ray optics made it possible to image a number of known SNRs in M33, and to perform a search for new ones (though few new SNRs were found). The number of new SNRs discovered in X-rays is small because (a) optical CCD technology enabled sensitive searches for extragalactic SNRs well before X-ray technology began to catch up, and (b) most SNRs in even nearby galaxies are faint X-ray sources; even with observing times approaching $\sim 10^6$ s, there are insufficient (typically 10–100) counts to characterize the spectra of a source as that of an SNR or to measure the spatial extent.

Many SNRs have been identified as soft X-ray sources that are spatially coincident with objects in an independently derived catalog. Alternatively, "forced photometry" may also be used to extract the X-ray fluxes (or upper limits) for SNRs that have been identified optically. For M33, Long10 used forced photometry on the *Chandra* ACIS data of the 137 then-known SNRs to report 2σ detections of 82 objects, 58 of them at $>3\sigma$. *XMM-Newton* has greater sensitivity than *Chandra* and a larger field of view, but its angular resolution is not high enough to resolve SNRs in confused regions. Garofali et al. 2017 used forced photometry to detect 105 objects in the larger SNR sample discussed here, at 3σ. The typical X-ray luminosity of the objects detected by Garofali et al. (2017) was 7×10^{34} erg s^{-1} (0.2–2 keV) at the distance of M33. In total, there are 112 objects that were detected at 3σ in one or both X-ray studies. We take these to be the X-ray detected sample of SNRs in M33, and have recorded this in Table 1.

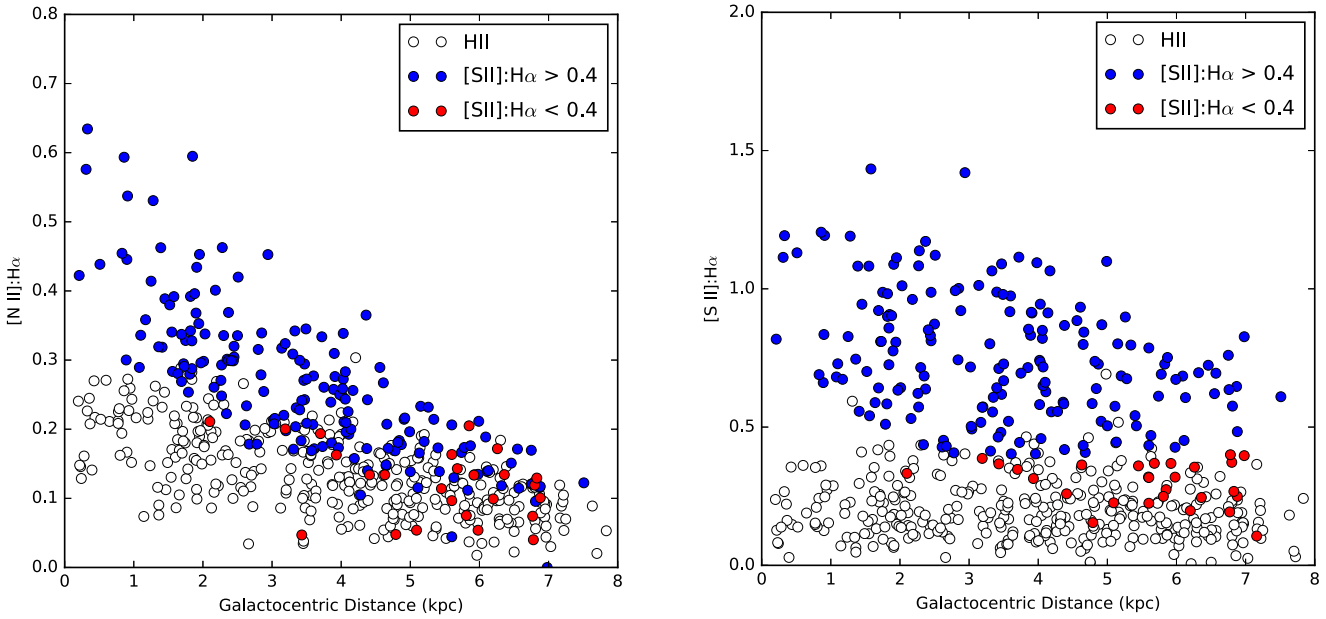

Figure 10. The [N II]:Hα ratios (left) and [S II]:Hα ratios (right), as a function of galactocentric distance. In this case, we have separated the SNR candidates into to those that have [S II]:Hα ratios greater or less than 0.4. The H II region ratios are also plotted.

Of these objects, 106 also have [S II]:Hα ratios of greater than 0.4.[12] It may be tempting to select these 106 objects as bona fide SNRs, and treat objects that have only a high [S II]:Hα ratio as more suspect. In general, that is a viewpoint we support. However, one should be aware that, while these 106 objects may be the purest subsample of SNRs among the candidates, many Galactic SNRs would not have been detected in X-rays at the distance of M33, so this subsample is by no means complete. Furthermore, given that many of the X-ray detections are near 3σ, and at this limit it is sometimes difficult to separate a SNR from a peak in the X-ray background, X-ray detection is not always sufficient to authenticate an SNR candidate (see discussion in Long10).

Radio observations offer an additional means of verifying SNR candidates. Unfortunately, the most recent radio survey of SNRs in M33 was by Gordon et al. (1999), which targeted 98 SNR candidates that had been identified in Gordon et al. (1998). Of that list, Gordon et al. (1999) claimed radio detections of 53. A new radio survey of M33 using JVLA observations is currently underway (see Long et al. 2016; R. L. White et al. 2018, in preparation) and should be a major step forward, both in confirming candidate objects and in elucidating the relationships among X-ray, optical, and radio emission from SNRs.

4.4. Variation of Line Ratios with Galactocentric Distance

The large number and high quality of spectra now available for both SNRs and H II regions in M33 allows us to revisit the situation with observed line ratios as a function of GCD. Figure 10 shows the variation of both [N II]:Hα and [S II]:Hα as a function of GCD, with different symbols for the SNR samples and H II regions.[13] Three general aspects are immediately obvious: (1) the ratios are generally significantly higher in the SNR sample compared with H II regions; (2) this separation is more dramatic near the inner part of the galaxy (i.e., there is a stronger gradient in line ratio with GCD for the SNRs, and more potential confusion at larger GCDs); and (3) there is a significant dispersion in ratio values within each object class at a given GCD. These trends have been noted previously, although the larger sample size here makes them more obvious.

The trends of the two line ratios with GCD show somewhat different behavior for SNRs than for H II regions and the two line ratios themselves. For the SNR sample, both line ratios show a gradient, with decreasing values at larger GCD, despite the considerable dispersion. For the H II regions, a more modest gradient is seen in [N II]:Hα, and it is not clear that any gradient is present for the [S II]:Hα ratio. The absence of a gradient in the [S II]:Hα ratio in H II regions is probably due to the fact that most S in H II regions is more highly ionized; decreasing line ratios of [S III] and [S IV] to hydrogen are observed in the IR, and have been taken to imply an S abundance gradient of $d\log(\mathrm{S/H})/dR$ of -0.052 ± 0.021 dex kpc^{-1} (Rubin et al. 2008). The general offset in each ratio between the SNRs and H II regions has been seen many times before and is attributable to the differing excitation mechanisms between the two classes of objects (see Blair et al. 1982; Kewley & Dopita 2002; Allen et al. 2008).

In addition to showing trends, it is quite apparent in the large samples of both H II regions and SNRs that there is considerable dispersion in ratio values at a given GCD. Given the high quality of the spectra, most of this dispersion must arise from abundance variations, varying physical conditions

[12] The six outliers are L10-035, L10-040, LL14-005, LL14-008, LL14-134, and LL14-162. Of these, L10-035 and L10-040 had previously published spectra. For L10-035, Long10 reported a ratio of 0.36, not too different from what we report now, so this object does not appear to satisfy the formal criterion of 0.4 for an SNR. For L10-040, the spectrum is from Smith et al. (1993), who found an [S II]:Hα ratio of 0.65, whereas we find 0.33. L10-040 has a fairly complete shell 55 pc in diameter; it is probable that the difference in ratios is due to the placement of the Hectospec fiber compared to the slit used by Smith et al. (1993). At any rate, new spectra of all of these objects would be desirable.

[13] We note, for the record, that a similar plot for [O I]:Hα shows no trend with GCD for either SNRs or H II regions.

within the emitting plasmas of each type of object, or some combination of the two. Because most, if not all, of the SNRs identified in M33 have swept up much more mass from the ISM than was ejected by the SN, and none of the spectra show direct evidence of ejecta, the actual abundances (and any variations) in the H II regions and SNRs should be similar, reflecting that of the ISM.

Rosolowsky & Simon (2008) and Magrini et al. (2010) have both investigated H II region abundances in M33 with significant (albeit somewhat smaller) samples of H II regions (and planetary nebulae, in the case of the latter paper), and found evidence for both overall abundance gradients and abundance variations (primarily O abundances, but also N) within averaged GCD bins. (Sulfur abundances were not addressed.) Lin et al. (2017) used their extensive observations to derive an inverse temperature gradient and the O abundance gradient in M33 via several different diagnostic ratios. A similar analysis is also available for a large sample of H II regions in M31 that also show variation in derived abundances at a given GCD (Sanders et al. 2012). Both sets of authors claim a certain amount of variation in derived abundances at a given GCD, with Rosolowsky & Simon (2008) claiming azimuthal variation within a given GCD bin (cf. Bresolin (2011) and Magrini et al. (2010), who show that bright giant H II regions have a steeper abundance gradient than the remainder of their sample). Unless one wants to believe that the actual abundances are different in these different objects, the proper inference here may be that ionization differences between the bright H II region sample and fainter, more normal H II regions are responsible for different derived abundance values.

The key issue in interpreting Figure 10 is the nature of the dispersion in ratios observed in the different classes of objects. Large grids of H II region models, such as those of Kewley & Dopita (2002) and Vale Asari et al. (2016) show that variations in the ionization parameter can affect the observed line ratios, but abundance variations can impact observed ratios as well. Likewise, for shock models (Allen et al. 2008), we recently conducted a careful assessment for M83 SNRs (Winkler et al. 2017) and concluded that both abundance variations and variations in reasonable assumptions for the shock conditions could contribute to the observed spread in line ratios.

From the results of Magrini et al. (2010), it is tempting to assign a surface brightness variation as a surrogate for mean ionization of an H II region. Referring back to Figure 8 (right), the increase in [S II]:Hα ratio at lower surface brightnesses may be a manifestation of the same effect, and thus causing the uncertainty in object identifications based on this ratio. However, as seen in Figure 8 (left), the [N II]:Hα ratio versus surface brightness shows some dispersion but a much smaller trend with surface brightness, indicating that little of the [N II]:Hα dispersion can be attributed to this same effect.

In an attempt to shed some light on whether physical conditions or abundance variations explain the variations in the line ratios seen in the spectra of SNRs, we have compared the observed line ratios to the ratios shown in the grid of MAPPINGS III shock models presented by Allen et al. (2008). An example of this comparison is shown in the left panel of Figure 11 for [O III] λ5007:Hβ as a function of [N II] λ6584:Hα. For reasons discussed below, the grids we have elected to show are for shocks without precursors for models with Small Magellanic Cloud (SMC), Large Magellanic Cloud (LMC), and solar abundances.[14] Each of the grids is for a shock propagating into an ISM with a density of 1 cm^{-3}. Each grid covers a range of shock velocities from 100 to 1000 km s^{-1} and a range of pre-shock magnetic fields from 10^{-4} to 10 μG. As such, the model grids were intended to cover the range of plausible conditions for radiative shocks propagating into an ISM with different metallicities. There will, of course, be some old SNRs with shock speeds below 100 km s^{-1}, and those may account for some of the fainter objects with weak [O III] emission. Also, SNRs with primary shocks faster than 500 km s^{-1} are unlikely to have reached the radiative stage, so unless the primary shock has driven secondary shocks into denser knots of the ISM, they may be underrepresented in the sample.

As shown in Figure 11, there is a clear separation in the three model grids in the [N II]:Hα ratios, while variation in terms of [O III]:Hβ is not as great. The line ratios that we observe from SNRs and SNR candidates in M33 show considerable scatter but cluster around the values seen in LMC grid. The log of the O abundance relative to H for M33 is -3.6 to -3.7 (e.g., Lin et al. 2017); the O abundance in the LMC grid is -3.65, so it is comforting that the observations cluster near the LMC grid. There are 3.8 times as many O atoms in the grid with solar abundances and 2.1 times fewer in the grid with SMC abundances. The fact that there is an overall trend toward weaker [N II]:Hα ratios with GC distance is consistent with there being an abundance gradient in M33.

The left panel of Figure 12 shows a similar comparison for the ratio of [N II]:Hα as a function of the ratio of [S II]:Hα. The same three model grids are shown. Once again, most of the data clusters near the LMC model grid. If one concentrates on just the distribution along the [S II]:Hα axis, it is fairly clear that much more of the variation in the expected [S II]:Hα ratios arises from differences in the models; i.e., differences in physical conditions rather than in the abundance.

As mentioned above, Figure 11 compares our line ratios with sets of Allen et al. (2008) models that do not include the contribution of the photoionization precursor. This is because the models that include the calculated precursor give poor agreement with the observations, in the sense that the models including the precursor predict [O III]:Hβ ratios higher than observed, by a factor of 2 or 3. This is because the low density in the precursor and the high ionizing flux from the shock imply a relatively high ionization state, and the emission is similar to that of an H II region.

The apparent weakness of the precursor contribution requires some explanation, as shocks faster than about 100 km s^{-1} produce substantial fluxes of ionizing photons. The precursors produced by the ionizing flux are observed as faint, diffuse emission outside several Galactic SNRs (e.g., Medina et al. 2014), but the surface brightness is so low that they make a miniscule contribution to the spectra from the bright, radiative SNR filaments. SNRs in the LMC are observed at much lower effective spatial resolution, so the relative contribution of the precursor can be correspondingly larger. Vancura et al. (1992) separated the pre-shock and post-shock components of the lines of N49, based on the velocity shifts and widths, and found that 18% of the [O III] and 5% of Hα originate in the precursor. At the still-greater distance of M33, one

[14] In the nomenclature of Allen et al. (2008), these are grids P, Q, and T for the SMC, LMC, and Galaxy, respectively.

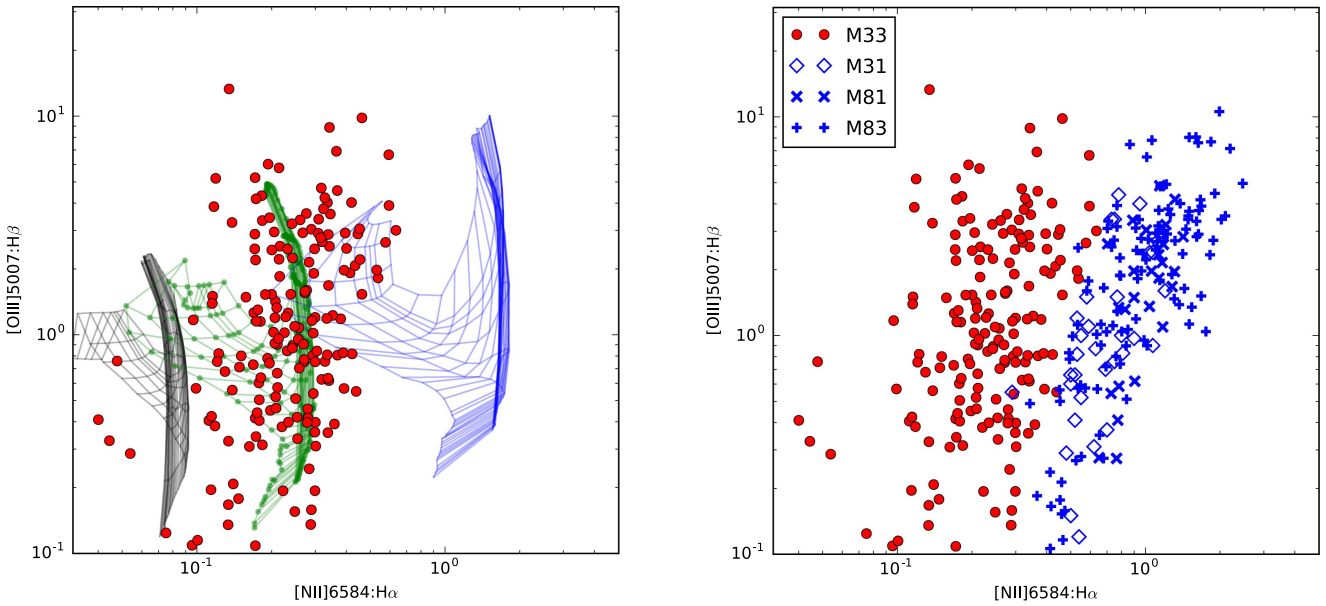

Figure 11. Left: Observed and model [O III] λ5007:Hβ ratio as function of the [N II] λ6583:Hα line ratio for SNRs and SNR candidates with spectra. As discussed in the text, the black, green, and blue meshes correspond to shock models with a range of shock velocities and pre-shock magnetic fields, and with metallicities corresponding to the SMC, LMC, and Milky Way, respectively. Right: Observed ratios of the same lines for SNRs and SNR candidate samples in M31, M81, and M83, as well as M33. The ratios for M31, M81, and M83 were taken from Galarza et al. (1999), Lee et al. (2015), and Winkler et al. (2017), respectively.

might expect even more of the precursor emission would be captured in the 6 pc effective size of the Hectospec fibers.

The reason that the precursor contribution is weaker than the model prediction is that the models assume planar geometry and steady-state emission. Cox (1972) showed that a typical SNR begins to radiate a significant part of its energy when the shock speed slows to around 300 km s^{-1}. It then emits a huge burst of ionizing photons as the speed declines further to around 100 km s^{-1}. The cooling and recombination time in the photoionized gas is long, compared to the time over which the SNR evolves, so only a fraction of the precursor emission is produced during the apparent lifetime of the SNR. As the shock slows further still, shocks with speeds around 50 km s^{-1} moving in relic photoionization precursors should produce relatively faint emission with modest [O III]:Hβ ratios, low densities, and small line widths.

4.5. Comparison to SNR Samples in Other Galaxies

Although M33 may have the best-studied SNR sample of any spiral galaxy, significant numbers of SNRs and SNR candidates have been identified in many other galaxies, including M31 (156, Lee & Lee 2014a), M83 ($\sim$300, Blair et al. 2012, 2014), and NGC 2403 (149, Leonidaki et al. 2013), all using the [S II]:Hα ratio as the primary criterion.

For M83, Winkler et al. (2017) obtained spectra of 118 candidates identified as having high [S II]:Hα ratios from interference filter images, and they confirmed the high ratio in all but one. With the notable exceptions of SN1957D (Long et al. 1989, 2012) and a very young SNR identified by Blair et al. (2015), none of the optical spectra show the broad lines expected from a Cas A analog. This is true even though M83 has 41 objects (22 with spectra) with *HST*-measured diameters less than 0.″5 (11 pc at $D = 4.6$ Mpc. At a diameter of 11 pc, the primary shock velocity of a remnant from a 10^{51} erg explosion expanding into an ISM with density 1 cm^{-3} would be $\sim$1800 km s^{-1}. According to Long et al. (2014), at least 87 of the approximately 300 optically identified SNR candidates in M83 have X-ray counterparts. As in M33, smaller diameter candidates are more likely to be X-ray-detected and to show higher densities from the ratios of the [S II] lines. As in M33, there is no evidence that the X-ray-detected objects differ from the non-detected objects in terms of reddening. However, trends of [N II]:Hα and [S II]:Hα with GCD are less obvious in M83 than in M33, a fact that Winkler et al. (2017) argue is due to local abundance variations. For a given [S II]:Hα ratio, the [N II]:Hα ratio is higher in M83 than M33, which almost certainly reflects the higher metallicity of M83. This is illustrated in the right panels of Figures 11 and 12, where the data points taken from Winkler et al. (2017) are well-separated from the locus of points for M33.

M83, where the original sample of SNR candidates was identified using interference filter images taken in exquisite seeing ($\lesssim$0.″5) from *Magellan*, as well as from *HST*, is an example of a galaxy where one can be reasonably certain that the majority of the objects in the sample are SNRs. By contrast, NGC 2403, a spiral somewhat similar to M33 but at a distance of 3.2 Mpc, is an example of a galaxy where a large number of candidates have been identified, but (despite the best efforts of Leonidaki et al. 2013) the sample is likely to be significantly contaminated by objects that are not actually SNRs. To create their sample, Leonidaki et al. (2013) used images with seeing that ranged from 1.″3 to 2.″5, corresponding to 20–40 pc at the distance of NGC 2403, on a modest-sized (1.3 m) telescope. They found 149 candidates, 102 of which had imaging-derived [S II]:Hα ratios $>$0.4, and 47 with ratios between 0.3 and 0.4. They obtained spectra of 22 of the objects; while 7 of the 8 objects with imaging ratios between 0.3 and 0.4 turned out to have spectroscopic [S II]:Hα ratios greater than 0.4, only 5 of 14 objects with imaging ratios $>$0.4 had spectroscopic ratios $>$0.4. Only about 40 ks of *Chandra* imaging exists for NGC 2403 (compared to 730 ks for M83), and so although Leonidaki et al. (2013) note that 6 of the 149 candidates are spatially coincident with X-ray sources in NGC 2403, all of these have hard X-ray spectra and are likely to be X-ray

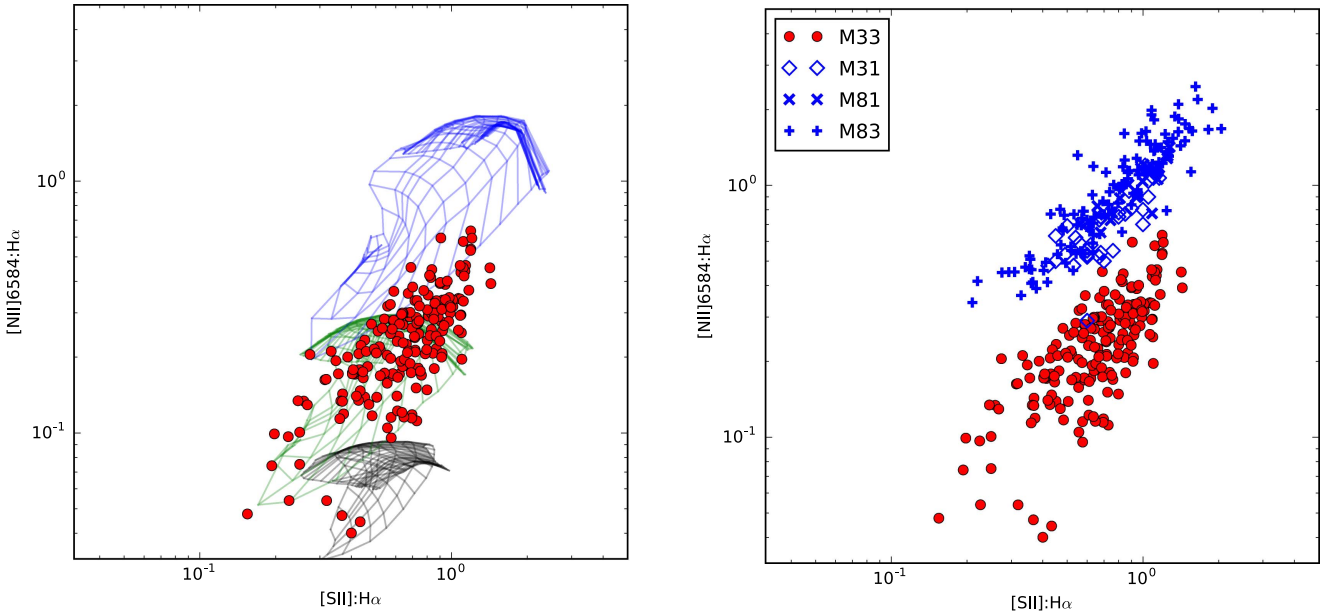

Figure 12. Similar to Figure 11, except here the [N II] λ6583:Hα ratio is plotted as a function of the [S II]:Hα ratio.

binaries (though Leonidaki et al. 2013 also mention the possibility that these could be Crab-like SNRs). Thus, whether or not a [S II]:Hα ratio of 0.4 should qualify an emission nebula as a SNR candidate, near-complete samples of SNRs in nearby galaxies require high-quality optical data with the best spatial resolution possible, spectroscopic follow-up on large telescopes, and if possible, deep X-ray observations at the resolution provided by *Chandra*.

M31 is a galaxy where the quality of the existing SNR catalogs is probably in an intermediate state between the relative completeness of M33 and M83, and the incomplete state of NGC 2403. Following early studies of M31 carried out with photographic plates, the first SNR search using CCDs, by Braun & Walterbos (1993), was limited to portions of the northwestern half of the galaxy. A subsequent study, by Magnier et al. (1995), covered a larger fraction of M31, but did not use continuum-subtracted images nor attempt any quantitative measurement of the [S II]:Hα ratio. By far the most thorough search for SNRs in M31 was done by Lee & Lee (2014a), in a companion study to the LL14 study of M33 that was similarly based on LGGS images. They identified 156 SNR candidates, of which 76 were newly discovered by their study. At first, it may seem surprising that similar searches yielded over 25% more candidates in M33 than in the much larger M31.

As in M83 (but less so in M33), the SNR candidates in M31 are preferentially located in the spiral arms and ring structure, where most of the star formation is taking place. Despite the fact that M31 is much more massive than M33, the star formation rates (SFR) in M31 ($0.4\,M_\odot\,\mathrm{yr}^{-1}$; Barmby et al. 2006) and M33 ($0.45 \pm 0.1\,M_\odot\,\mathrm{yr}^{-1}$; Verley et al. 2009) are comparable. One would expect the number of SNe to scale roughly in accord with the SFR, and hence that M31 and M33 would have comparable numbers of SNRs. The fact that surveys of M33 by Long10 and LL14, and of M31 by Lee & Lee (2014a), based on similar LGGS images of the two galaxies, have revealed ∼50% more SNRs in M33 than in M31 is probably attributable to the fact that M31 is more inclined and more highly reddened than M33. Lee & Lee (2014a) required all objects to have an integrated [S II]:Hα ratio (from the LGGS images) strictly >0.4 to be in their catalog; the mean ratio is 0.8. As in the case of M83, the [S II]:Hα ratios in M31 show only a slight gradient with GCD, and a large scatter. Only 23 of the objects in the M31 optical sample are in the XMM catalog of M31 SNRs presented by Sasaki et al. (2012), but no one has yet carried out a study like that of Long10 or Garofali et al. (2017) where the positions of the SNR candidates were searched for X-ray emission using forced photometry.

The main question about the optical sample in M31 is similar to that for the M33 sample: What fraction of the objects are actually SNRs? The problem is worse in M31 than M33, however, because in the case of M31, there has been no systematic attempt to obtain spectra, and hence line ratios for the complete sample, and the surface brightness of the M31 sample (see Figure 18 of Lee & Lee 2014a) extends to even fainter values than for M33. Spectroscopic follow-up for the SNRs is needed, to confirm the [S II]:Hα ratios derived from imaging and compare those ratios with H II regions of similar surface brightness. Spectra do exist for at least 33 SNRs in M31 (Galarza et al. 1999), and as in the case of M83 (see the right panels of Figures 11 and 12), they lie in regions of the ratio diagrams expected for solar-like abundances.

5. Summary

We have obtained spectra of 197 SNRs and SNR candidates in M33, using the Hectospec fiber-fed spectrograph at the 6.5 m MMT Observatory at Mt. Hopkins. These spectra cover the great majority of such objects listed in recent catalogs by L10 and LL14. Of these, 110 appear in both catalogs, while 18 are in L10 only and 69 are in LL14 only, for a total of 217. These data were analyzed and compared to a subset of H II regions recently published in Lin17. Our principal results are as follows:

1. Fits to the emission-line spectra show that the flux ratio of [S II] λλ6717, 6731:Hα is above 0.4 for 170 of the 197 objects. Traditionally, a value for the [S II]:Hα ratio >0.4 has been taken as the principal optical diagnostic for

shock-heated material, such as that found in SNRs, while photoionized nebulae have usually been found to have significantly lower values. If we take into account the eight objects that we did not observe, but for which archival spectra exist, then 178 of the 217 objects proposed to be SNRs have an [S II]:Hα ratio >0.4. The 39 objects that either have not been observed spectroscopically or appear to have ratios less than 0.4 should be regarded as questionable, at least until adequate spectra are obtained.

2. While the majority of the emission nebulae in the SNR candidate lists that have high [S II]:Hα ratios are almost certainly SNRs, a comparison of the line ratios from the SNR sample to the H II region sample of Lin17 shows H II region [S II]:Hα ratios that are rising as the surface brightness decreases. Thus, it is apparent that the [S II]:Hα ratio criterion alone is not completely reliable for distinguishing between these two classes of nebulae. The [O I]:Hα line ratio provides further confirmation that many candidates with [S II]:Hα > 0.4 are indeed SNRs, but adds no new objects, primarily because the [O I] lines are weaker than the [S II] ones and are confused with night sky emission. Furthermore, some of the fainter H II regions have [O I]:Hα ratios that overlap with those seen in comparably faint SNR candidates.
3. In an attempt to develop a clean sample of SNRs from optical criteria only, another potential discriminant is the velocity broadening of the emission lines. The bright H II regions that we observed all have line widths that are consistent with the instrumental width, whereas widths we measure for the SNR candidates are notably broader. However, the spectral resolution of Hectospec ($\sim$5 Å) is not sufficient to effectively separate SNRs with shocks $\lesssim$200 km s^{-1} from H II regions. Higher-resolution spectra would, in principle, provide an effective discriminant. They would also provide important information about shock velocities and the evolutionary state of the small diameter SNRs, but obtaining them with high S/N for faint objects would require a significant investment of telescope time.
4. Of the 217 optical SNRs and candidates in the catalog compiled here, 112 have been detected at 3σ or higher in one or both of the recent deep X-ray surveys from *Chandra* (Long et al. 2010) and *XMM-Newton* (Garofali et al. 2017). Of these 112 objects, 106 have [S II]:Hα ratios greater than 0.4.
5. The SNRs show a strong radial gradient in both the [N II]:Hα and [S II]:Hα ratios, decreasing at larger distances from the galaxy's center. As concluded by previous studies that have observed similar gradients in M33 with far smaller samples, these are almost certainly due to decreasing elemental abundances with larger GCD. The H II region sample shows a similar, albeit milder gradient in [N II]:Hα, but the [S II]:Hα ratio is essentially flat with GCD.
6. The substantial samples of both SNRs and H II regions with high-quality spectra also allow us to confirm a large dispersion in these line ratios at a given GCD. Comparison to models indicates that both varying physical conditions and varying abundances contribute to this spread in observed ratios.
7. The line ratios seen in the SNR sample of M33 are consistent with those predicted by shock models expanding into an ISM with the metallicity of M33, but only if precursor radiation is modest. Spectra of SNRs in other galaxies, such as M31 and M83, have higher line ratios that reflect their higher metallicity.

In order to fully understand the population of SNRs in M33 and other nearby galaxies, we would ideally like to compare SNR samples identified independently from deep surveys in the optical, X-ray, and radio bands. The current study is at least close to what can be achieved optically with current instruments. One might try to create a "gold standard" of optically identified SNRs, but this has the disadvantage that it would exclude a number of actual SNRs (especially fainter ones), so we have elected not to attempt this. Deep observations from *Chandra* (Long et al. 2010) and *XMM-Newton* (Garofali et al. 2017) have successfully detected a majority of M33's SNRs, though there are doubtless others whose X-ray flux falls below the detection threshold of those studies. Deeper X-ray observations of M33 are unlikely to be forthcoming with the current generation of X-ray observatories, especially since the soft X-ray sensitivity of the ACIS instrument on *Chandra* has declined due to the build-up of contamination on the detector filter. However, deeper and more complete radio studies than that of Gordon et al. (1999) are definitely practicable with current instruments, and we are currently pursuing this goal.

Observations reported here were obtained at the MMT Observatory, a joint facility of the Smithsonian Institution and the University of Arizona. P.F.W. acknowledges support from the NSF through grant AST-1714281. W.P.B. acknowledges ongoing support from the JHU Center for Astrophysical Sciences. We also appreciate the support in the form of Hectospec observations provided by Nelson Caldwell, and valuable comments made by Paul P. Plucinsky on the paper prior to submission.

Facility: MMT (Hectospec).

Software: astropy (Astropy Collaboration et al. 2013).

ORCID iDs

Knox S. Long https://orcid.org/0000-0002-4134-864X
William P. Blair https://orcid.org/0000-0003-2379-6518
Dan Milisavljevic https://orcid.org/0000-0002-0763-3885
John C. Raymond https://orcid.org/0000-0002-7868-1622

References

Allen, M. G., Groves, B. A., Dopita, M. A., Sutherland, R. S., & Kewley, L. J. 2008, ApJS, 178, 20
Astropy Collaboration, Robitaille, T. P., Tollerud, E. J., et al. 2013, A&A, 558, A33
Barmby, P., Ashby, M. L. N., Bianchi, L., et al. 2006, ApJL, 650, L45
Blair, W. P., Chandar, R., Dopita, M. A., et al. 2014, ApJ, 788, 55
Blair, W. P., & Kirshner, R. P. 1985, ApJ, 289, 582
Blair, W. P., Kirshner, R. P., & Chevalier, R. A. 1982, ApJ, 254, 50
Blair, W. P., & Long, K. S. 1997, ApJS, 108, 261
Blair, W. P., Winkler, P. F., & Long, K. S. 2012, ApJS, 203, 8
Blair, W. P., Winkler, P. F., Long, K. S., et al. 2015, ApJ, 800, 118
Braun, R., & Walterbos, R. A. M. 1993, A&AS, 98, 327
Bresolin, F. 2011, ApJ, 730, 129
Cox, D. P. 1972, ApJ, 178, 159
D'Odorico, S., Benvenuti, P., & Sabbadin, F. 1978, A&A, 63, 63
Dopita, M. A., D'Odorico, S., & Benvenuti, P. 1980, ApJ, 236, 628
Dopita, M. A., & Sutherland, R. S. 1995, ApJ, 455, 468
Fabricant, D., Fata, R., Roll, J., et al. 2005, PASP, 117, 1411
Freedman, W. L., Madore, B. F., Gibson, B. K., et al. 2001, ApJ, 553, 47

Galarza, V. C., Walterbos, R. A. M., & Braun, R. 1999, AJ, 118, 2775
Garofali, K., Williams, B. F., Plucinsky, P. P., et al. 2017, MNRAS, 472, 308
Gordon, S. M., Duric, N., Kirshner, R. P., Goss, W. M., & Viallefond, F. 1999, ApJS, 120, 247
Gordon, S. M., Kirshner, R. P., Long, K. S., et al. 1998, ApJS, 117, 89
Hartigan, P., Raymond, J., & Hartmann, L. 1987, ApJ, 316, 323
Hoopes, C. G., Walterbos, R. A. M., & Bothun, G. D. 2001, ApJ, 559, 878
Kewley, L. J., & Dopita, M. A. 2002, ApJS, 142, 35
Lee, J. H., & Lee, M. G. 2014a, ApJ, 786, 130
Lee, J. H., & Lee, M. G. 2014b, ApJ, 793, 134
Lee, M. G., Sohn, J., Lee, J. H., et al. 2015, ApJ, 804, 63
Leonidaki, I., Boumis, P., & Zezas, A. 2013, MNRAS, 429, 189
Levenson, N. A., Kirshner, R. P., Blair, W. P., & Winkler, P. F. 1995, AJ, 110, 739
Lin, Z., Hu, N., Kong, X., et al. 2017, ApJ, 842, 97
Long, K. S. 2017, arXiv:1712.05331
Long, K. S., Blair, W. P., Godfrey, L. E. H., et al. 2012, ApJ, 756, 18
Long, K. S., Blair, W. P., Kirshner, R. P., & Winkler, P. F. 1990, ApJS, 72, 61
Long, K. S., Blair, W. P., & Krzeminski, W. 1989, ApJL, 340, L25
Long, K. S., Blair, W. P., Winkler, P. F., et al. 2010, ApJS, 187, 495
Long, K. S., Kuntz, K. D., Blair, W. P., et al. 2014, ApJS, 212, 21
Long, K. S., White, R. L., Becker, R. H., et al. 2016, Supernova Remnants: An Odyssey in Space after Stellar Death (Chania, Greece), 9
Magnier, E. A., Prins, S., van Paradijs, J., et al. 1995, A&AS, 114, 215
Magrini, L., Stanghellini, L., Corbelli, E., Galli, D., & Villaver, E. 2010, A&A, 512, A63
Massey, P., McNeill, R. T., Olsen, K. A. G., et al. 2007, AJ, 134, 2474
Massey, P., Olsen, K. A. G., Hodge, P. W., et al. 2006, AJ, 131, 2478
Medina, A. A., Raymond, J. C., Edgar, R. J., et al. 2014, ApJ, 791, 30
Milisavljevic, D., Fesen, R. A., Chevalier, R. A., et al. 2012, ApJ, 751, 25
Osterbrock, D. E., & Ferland, G. J. 2006, Astrophysics of Gaseous Nebulae and Active Galactic Nuclei (2nd ed.; Sausalito, CA: Univ. Science Books)
Raymond, J. C. 1979, ApJS, 39, 1
Reynolds, R. J. 1985, ApJ, 294, 256
Rosolowsky, E., & Simon, J. D. 2008, ApJ, 675, 1213
Rubin, R. H., Simpson, J. P., Colgan, S. W. J., et al. 2008, MNRAS, 387, 45
Sanders, N. E., Caldwell, N., McDowell, J., & Harding, P. 2012, ApJ, 758, 133
Sasaki, M., Pietsch, W., Haberl, F., et al. 2012, A&A, 544, A144
Smith, R. C., Kirshner, R. P., Blair, W. P., Long, K. S., & Winkler, P. F. 1993, ApJ, 407, 564
Tüllmann, R., Gaetz, T. J., Plucinsky, P. P., et al. 2008, ApJ, 685, 919
Tüllmann, R., Gaetz, T. J., Plucinsky, P. P., et al. 2011, ApJS, 193, 31
Vale Asari, N., Stasińska, G., Morisset, C., & Cid Fernandes, R. 2016, MNRAS, 460, 1739
Vancura, O., Blair, W. P., Long, K. S., & Raymond, J. C. 1992, ApJ, 394, 158
Verley, S., Corbelli, E., Giovanardi, C., & Hunt, L. K. 2009, A&A, 493, 453
Williams, B. F., Wold, B., Haberl, F., et al. 2015, ApJS, 218, 9
Winkler, P. F., Blair, W. P., & Long, K. S. 2017, ApJ, 839, 83
Wood, K., Hill, A. S., Joung, M. R., et al. 2010, ApJ, 721, 1397